HHS Public Access

Author manuscript

Nat Mater. Author manuscript; available in PMC 2022 January 29.

Published in final edited form as:

Nat Mater. 2021 November ; 20(11): 1559–1570. doi:10.1038/s41563-021-01051-x.

Photocurable bioresorbable adhesives as functional interfaces between flexible bioelectronic devices and soft biological tissues

Quansan Yang[#1,2,3], **Tong Wei**[#4], **Rose T. Yin**[#5], **Mingzheng Wu**[#6], **Yameng Xu**[#7,8], **Jahyun Koo**[9], **Yeon Sik Choi**[1,2,7], **Zhaoqian Xie**[10,11,12], **Sheena W. Chen**[13], **Irawati Kandela**[14,15], **Shenglian Yao**[16], **Yujun Deng**[3,17], **Raudel Avila**[3], **Tzu-Li Liu**[3], **Wubin Bai**[1,2,7,18], **Yiyuan Yang**[1,2,3], **Mengdi Han**[1,2], **Qihui Zhang**[7], **Chad R. Haney**[15,19,20], **K. Benjamin Lee**[13], **Kedar Aras**[5], **Tong Wang**[4], **Min-Ho Seo**[1,2,7,21], **Haiwen Luan**[1,2,3], **Seung Min Lee**[7], **Anlil Brikha**[15,19], **Nayereh Ghoreishi-Haack**[14], **Lori Tran**[14,15], **Iwona Stepien**[14,15], **Fraser Aird**[15], **Emily A. Waters**[15,19,20], **Xinge Yu**[22], **Anthony Banks**[1,2], **Gregory D. Trachiotis**[5,23], **John M. Torkelson**[4,7], **Yonggang Huang**[1,3,7,24], **Yevgenia Kozorovitskiy**[6,15,*], **Igor R. Efimov**[5,*], **John A. Rogers**[1,2,3,7,20,25,*]

[1]Center for Bio-Integrated Electronics, Northwestern University, Evanston, IL 60208, USA

[2]Querrey Simpson Institute for Biotechnology, Northwestern University, Evanston, IL 60208, USA

[3]Department of Mechanical Engineering, Northwestern University, Evanston, IL 60208, USA

[4]Department of Chemical and Biological Engineering, Northwestern University, Evanston, IL 60208, USA

[5]Department of Biomedical Engineering, The George Washington University, Washington, DC, 20052, USA

[6]Department of Neurobiology, Northwestern University, Evanston, IL 60208, USA

[7]Department of Materials Science and Engineering, Northwestern University, Evanston, IL 60208, USA

[8]Institude of Materials Science and Engineering, Washington University in St. Louis, St. Louis, MO 63130, USA

[9]School of Biomedical Engineering, Korea University, Seoul 02841, Republic of Korea

[*]To whom correspondence should be addressed to yevgenia.kozorovitskiy@northwestern.edu (Y.K.), efimov@gwu.edu (I.R.E.), and jrogers@northwestern.edu (J.A.R.).

Author contributions

Q.Y., T.W., Y.K., I.R.E., and J.A.R. conceived the ideas and designed the research. Q.Y., T.W., Y.X., and T.L.L. synthesized and characterized the materials. Q.Y., Y.X., J.K., Y.S.C., W.B., Y.Y., M.H., Q.Z., M.H.S., S.M.L., and A.B. designed and fabricated the devices. R.T.Y., M.W., S.W.C., I.K., S.Y., C.R.H., K.B.L., K.A., A.B., I.S., F.A., E.A.W., and G.T. performed the *in vitro*, *ex vivo*, and *in vivo* studies. Q.Y., R.T.Y, Y.X., M.W., C.R.H., A.B., and E.A.W. performed the data analysis. Z.X., R.A., and Y.D. performed the mechanical and electrical modelling. Q.Y., Y.X., R.T.Y., T.W., M.W, J.M.T., Y.H., Y.K., I.R.E., and J.A.R. wrote the manuscript with input from all authors.

Competing interests

The authors declare no competing interests.

[10]State Key Laboratory of Structural Analysis for Industrial Equipment, Dalian University of Technology, Dalian, 116024, China

[11]Department of Engineering Mechanics, Dalian University of Technology, Dalian, 116024, China

[12]Ningbo Institute of Dalian University of Technology, Ningbo, 315016, China

[13]Department of Surgery, The George Washington University, Washington, DC 20052, USA.

[14]Developmental Therapeutics Core, Northwestern University, Evanston, IL 60208, USA.

[15]Chemistry Life Processes Institute, Northwestern University, Evanston, IL 60208, USA.

[16]School of Materials Science and Engineering, University of Science & Technology Beijing, Beijing 100083, China.

[17]State Key Laboratory of Mechanical System and Vibration, Shanghai Jiao Tong University, Shanghai 200240, China.

[18]Department of Applied Physical Sciences, University of North Carolina at Chapel Hill, NC 27599, USA.

[19]Center for Advanced Molecular Imaging, Northwestern University, Evanston, IL 60208, USA.

[20]Department of Biomedical Engineering, Northwestern University, Evanston, IL 60208, USA.

[21]School of Biomedical Convergence Engineering, College of Information & Biomedical Engineering, Pusan National University, Pusan 43241, Republic of Korea.

[22]Department of Biomedical Engineering, City University of Hong Kong, Hong Kong 999077, China.

[23]DC Veterans Affairs Medical Center, The George Washington University, Washington, DC 20052, USA.

[24]Departments of Civil and Environmental Engineering, Northwestern University, Evanston, IL 60208, USA.

[25]Department of Neurological Surgery, Feinberg School of Medicine, Northwestern University, Chicago, IL 60611, USA.

[#] These authors contributed equally to this work.

Abstract

Flexible electronic/optoelectronic systems that can intimately integrate onto the surfaces of vital organ systems have the potential to offer revolutionary diagnostic and therapeutic capabilities relevant to a wide spectrum of diseases and disorders. The critical interfaces between such technologies and living tissues must provide soft mechanical coupling and efficient optical/electrical/chemical exchange. Here we introduce a functional adhesive bioelectronic/tissue interface material, in the form of mechanically compliant, electrically conductive and optically transparent encapsulating coatings, interfacial layers, or supporting matrices. These materials strongly bond both to the surfaces of the devices and to those of different internal organs, with stable adhesion for several days to months, in chemistries that can be tailored to bioresorb at controlled rates. Experimental demonstrations in live animal models include device applications

that range from battery-free optoelectronic systems for deep-brain optogenetics and subdermal phototherapy to wireless millimeter-scale pacemakers and flexible multi-electrode epicardial arrays. These advances have immediate applicability across nearly all types of bioelectronic/optoelectronic systems currently used in animal model studies, and they also have the potential for future treatment of life-threatening diseases and disorders in humans.

Capabilities that follow from the intimate integration of high performance electronic/optoelectronic systems with soft living tissues have the potential to serve as the basis for revolutionary approaches to diagnosing and treating diseases[1-5]. A common vision is that a synergistic, bidirectional union of technology with biology will establish routes to improving health and prolonging life in ways that could complement those of traditional techniques. In all cases, the physical interfaces between these abiotic and biotic systems must enable soft mechanical coupling and functional optical/electrical/chemical exchange[6-8]. Structural techniques based on surgical sutures, staples, cuffs, or clips[9] have some utility but they induce damage to the tissues and the devices[10], and they often result in adverse immune responses[11,12] and mechanical instabilities. Such methods also support bonding only at discrete locations, leading to unreliable and/or inhomogeneous, time-varying contacts across the full interfacial area[13]. Existing adhesives for tissue repair[14-18], drug delivery[14], and wound dressings[19] may have utility, but these materials fail to satisfy all of the essential requirements for bioelectronic/tissue interfaces (detailed limitations in Supplementary Note 1 and Supplementary Table 1-2). The adhesive must provide robust adhesion, not only to biological tissues, but also to the surfaces of electronic devices with mechanical, geometrical, and chemical characteristics that are vastly different from those of the soft tissues. During the surgical process, the processes of applying and activating the interface materials must minimize deformations and damage to the tissues and the devices. Application must occur easily, across diverse classes of electronic systems, including those adopting three-dimensional layouts and/or complex surface topographical features[20]. To support functional electronic or optical exchange between devices and tissues, high light transmission and appropriate levels of ionic conductivity are also important[21-23]. For applications in bioresorbable electronics, the chemistries must accommodate designs that offer bioresorbability with rates that match use cases in temporary implants.

This paper introduces a functional adhesive, which we refer to as a bioelectronic/tissue interface material (BTIM), that meets the requirements outlined above. The BTIM combines photocurable covalent networks (PEG-LA-DA; Supplementary Fig. 1 and Note 2) with ionic networks (sodium alginate, SA) that quickly form upon application onto tissue/electronics surfaces. The result is a material with a honey-like initial viscosity that can flow to conform to complex surfaces. Chemical designs support robust bonding to both sides of the interface *in situ*. Conformal coverage across complex tissue/electronics surfaces enables multiple strategies to address diverse classes of biological tissues and electronic systems. Photopolymerization leads to a liquid-solid transformation and bonding without application of force, thereby facilitating surgical processes and reducing the potential for damage or excessive deformations of fragile tissues or delicate electronic devices. These BTIMs are highly transparent, with electrical conductivity that arises from motions of ions in the network, to meet requirements for wide ranging types of optoelectronic and bioelectronic

devices. The lactide acid units, along with the alginate and chitosan components, allow for controlled resorption entirely in the body through natural process at well-defined rates, thereby addressing opportunities in temporary implants that are designed to eliminate costs and risks of surgical removal procedures.

An important component of this work is a collection of demonstrations with diverse electronic/optoelectronic devices interfaced to the surfaces of different vital organs in the context of optical and electronic modes of stimulation and measurement in live animal models, from days and weeks to months. Examples include battery-free optoelectronic platforms that wirelessly deliver light stimuli to regions of the deep brain or subcutaneous tissues, stably and without inciting inflammation. In other experiments, the BTIM forms adhesive ‘tunnels’, or conduits, for interconnects/cables that join different components of implantable devices to span large distances across the anatomy. Further demonstrations highlight applicability to highly dynamic organs such as the heart, where wireless millimeter-scale pacemakers and high-density flexible multielectrode arrays mount directly onto the epicardial surfaces of rat models and Langendorff-perfused rabbit hearts. All of these BTIM-assisted bioelectronic/optoelectronic devices retain their functions and positions throughout the periods of study. These collective results highlight the broad spectrum of possibilities enabled by this class of adhesive material.

BTIM designs and characterizations

Fig. 1a presents a schematic illustration of the standard means for establishing interfaces by use of sutures, as a reference[9] for the methods introduced here (illustrations in Fig. 1b-d), where thin, soft layers of the BTIM serve as soft, transparent, and electrically conductive bonds to the targeted tissues. Suturing (Fig. 1a) typically requires multiple points of attachment via threads that penetrate the device and the tissue, thereby causing damage to both. The BTIM, by contrast, can be used as encapsulating coatings (Fig. 1b), interfacial layers (Fig. 1c), or supporting matrices (Fig. 1d) depending on the device architectures and application scenarios. The encapsulation technique involves casting and curing a liquid precursor of the BTIM onto the surface of a device to yield a coating that extends to the adjacent tissues. This scheme physically holds the device through chemical bonds formed with the surrounding tissue. In the interface method, the BTIM chemically bonds to the amine-functionalized bottom surface of the device, on one side, and to the tissue on the other. In the matrix scheme, the precursor flows around the three-dimensional structured device to form a solid, supportive, and protective matrix that can be joined to the surface of the tissue using the other two approaches. Photographs associated with the application of this two-component adhesive chemistry onto a porcine heart to anchor a pair of electrodes with an encapsulation coating scheme appear in Fig. 1e.

As shown in Fig. 1f, Extended Data Fig. 1 and Supplementary Fig. 2-3, this material system allows seamless integration of electronic and optoelectronic systems, including 3D platforms, onto the surfaces of living tissues, with robust adhesion for stable electrical and/or optical interfaces across dermal, neuronal, and cardiac applications for several days to months (detailed procedure in Supplementary Fig. 4).

Fig. 2a presents the mechanisms of bonding to the surfaces of biological tissues (first panel) and devices (second panel) through the use of primers. The primer for the tissue surfaces[15] consists of chitosan and coupling reagents (1-ethyl-3-(3-dimethylaminopropyl) carbodiimide (EDC) and sulfated N-hydroxysuccinimide (Sulfo-NHS)). The primary amine groups on the chitosan backbone covalently bond with carboxylic acid groups on the tissue surfaces and the alginate network to provide robust bonding, which is further enhanced by physical chain entanglement. The primer (EDC and Sulfo-NHS) for the devices promotes the reaction between amine groups functionalized onto device surfaces and carboxylic acid groups in the adhesive matrix. The amine groups (Supplementary Note 3) enable robust adhesion to the BTIM, with negligible influence on the device impedance (Extended Data Fig. 2). The combined effects of high cohesion energy (1900 J/m^2; Supplementary Note 4 and Supplementary Fig. 5) and strong bonding lead to high levels of adhesion strength, capable of addressing requirements for a wide variety of tissues and devices (Fig. 2b and Supplementary Fig. 6-7). Examples of bonding to wet tissue surfaces include the skin (300 ± 70 J/m^2), the epicardium (240 ± 20 J/m^2), the gastrointestinal wall (80 ± 30 J/m^2), the renal cortex (70 ± 10 J/m^2) and the hepatic lobule (50 ± 10 J/m^2). Bioelectronic surfaces include various encapsulation/substrate materials such as poly(lactic-co-glycolic acid) (PLGA; 260 ± 50 J/m^2), polylactic acid (PLA; 250 ± 50 J/m^2), polycaprolactone (PCL; 240 ± 40 J/m^2), parylene (120 ± 40 J/m^2), polyimide (PI; 110 ± 30 J/m^2) and polyurethane (PU; 90 ± 50 J/m^2).

Low modulus mechanical properties (Young's modulus: ~ 30 kPa) and high levels of elongation (up to 10 times) of the BTIM minimize stresses, and potential damage, at the tissue interfaces (Fig. 2c-d)[24,25]. Here, the material serves as a soft, strain isolation layer between devices and the tissues, with minimal normal and shear stresses associated with natural motions such as side-bending (angle: 45°) and bending-over (angle: 75°) analyzed by finite element analysis (FEA) (Fig. 2d and Supplementary Fig. 8-9). The strain isolating effects of the BTIM (thickness: 500 μm) decrease the stresses by up to a factor of 3.5, relative to that without the BTIM. Increasing the thickness of the BTIM further decreases these stresses (Supplementary Fig. 10).

Photoinitiated transformation from viscous liquid-type precursors to elastic crosslinked adhesives facilitates the formation of thin, conformal coatings directly on surfaces of interest. Fig. 2e presents the rheological behavior of the BTIM as a function of curing time. Free radial polymerization, initiated by UV exposure, yields a covalent network within 180 s (storage modulus, G', from 30 to 6000 Pa; tan δ, from 0.45 to 0.03). The initial storage modulus and viscosity (~ 2 – 3 Pa•s, similar to that of honey[26]; detailed information in Supplementary Fig. 11) are associated with the rapid formation of the alginate ionic network upon application onto tissue/electronics surfaces. The viscous characteristics prevent applied material from rapidly flowing away in an uncontrolled manner, to facilitate formation of spatially confined coatings with uniform thicknesses (detailed information in Supplementary Note 5). Applying and curing the BTIM in this fashion on porcine skin yields an interface that follows the natural texture of the tissue, as evidenced by inspecting the contacting surface following removal. Fig. 2f presents surface height profiles of the porcine skin (Ra: 13.27 μm; RMS: 16.88 μm) and the corresponding BTIM (Ra: 9.60 μm; RMS: 10.98 μm) along the white line in each corresponding 3D confocal optical image in the inset and

Supplementary Fig. 12. The strong correlation indicates that the liquid precursors wet and spread across rough tissue surfaces, thereby enhancing the adhesion strength by ensuring uniform contact. The photoinitiated gelation process also allows for casting onto highly structured and curved surfaces (detailed information in Supplementary Note 6). In fact, the precursors can completely fill the interior spaces of 3D bioelectronic systems without damaging fragile features, to achieve 3D electrode-embedded (Extended Data Fig. 1) and electrode-exposed (Supplementary Fig. 3) electronic structures.

The material is also bioresorbable through hydrolysis of lactide repeat units, aided by enzymatic reactions that can occur, as mediated by surrounding biofluids (Supplementary Note 7 and Supplementary Fig. 13). The lactide content determines the degradation lifetime, from ~ 20 days (PEG-10LA-DA system) to several months (PEG-2LA-DA system) in PBS (pH 7.4) at 37 °C in Fig. 2g. Such characteristics create opportunities for the use of the BTIM in the emerging area of bioresorbable electronic implants that support operation for a defined period of functional need and then disappear naturally[27]. Furthermore, multiple experiments establish cytocompatibility and biocompatibility (Supplementary Fig. 14-15 and Supplementary Note 8).

The optical transparency and the ionic conductivity of the BTIM are additional essential features as functional optoelectronic and electronic interfaces. The transmittance of the samples (thickness: 2 mm) is between 60 – 80% in the range of 395 to 475 nm, remains higher than 80% between 475 – 900 nm (Supplementary Fig. 16). The ionic conductivity is in the range of ~ 0.5 S/m at 1 kHz, similar to that of most biofluids. The BTIM can support bioelectronics for efficient local electrical stimulation and spatially resolved biopotential sensing. For electrical stimulation, a cardiac pacemaker serves as a representative example, shown in Fig. 2h. The normalized current in tissues and power consumption from Fig. 2i and Extended Data Fig. 3 suggest that the optimum conductivity for this scenario is 0.16 ~ 0.5 S/m, to avoid electrical connection block at low conductivity or electrical shorts at high conductivity. For biopotential sensing, a flexible multielectrode array (MEA) forms a representative example, shown in Fig. 2j. Fig. 2k and Extended Data Fig. 4 present the measured potential at the electrode on the left side as a function of conductivity, revealing that the optimum is 0.1 to 0.5 S/m. Such conductivities prevent signal attenuation at low conductivity and shorts at high conductivity. Experimental measurements on an ultra-thin, flexible multielectrode array (MEA; electrode dimensions: 500 μm × 500 μm; spacing: 1mm;) demonstrate these principles (Fig.2l and Supplementary Fig. 17). Representative impedance spectra between two adjacent MEA electrodes before (blue) and after (red) BTIM application (Fig. 2m) show negligible differences. Statistical results for impedance values before and after applying the BTIM are in Supplementary Fig. 18 are 8.6 ± 0.3 kΩ and 8.2 ± 0.3 kΩ, respectively, at 1 kHz in 0.1 M PBS at room temperature. The results together prove that the BTIM layer can act as an attractive interfacial material for bioelectronics without significant signal degradation. More generally, these studies also provide design guidelines for selecting the conductivity of an interface layer between bioelectronics devices and soft biological tissues. By using the proposed strategies, the need to pattern the interface materials is eliminated and any gap between tissue and electrode can be avoided.

Wireless light delivery systems for optical stimulation

As an example of the use of the BTIM with an integrated device, Fig. 3a presents a wireless light delivery system (10 mm × 6 mm × 300 μm) with potential applications in phototherapy. This device consists of an inductive loop antenna, an inorganic light-emitting diode (ILED), and associated electronic components. The BTIM encapsulation coating (12 mm × 8 mm × 500 μm) secures the device to the dorsal subcutaneous area in a mouse model, as shown in Fig. 3b, with stable device operation during natural movements (Supplementary Video 1). Fig. 3c demonstrates wireless activation of red (peak wavelength: 630 nm) and green (peak wavelength: 530 nm) ILEDs, selected for their relevance in tumor irradiation[28]. The BTIM fixes the positions of implanted devices for at least several months. Evaluating the positions of encapsulated devices (12 mm × 8 mm × 500 μm) by micro-computed tomography (MicroCT) along the diagonal (main), sagittal (first inset), and coronal (second inset) directions across day 2, 5, and 8 post-surgery quantifies the positional stability, as shown in the first row of Fig. 3d. Within experimental uncertainties, the devices remain in their original locations throughout the period of study. Similar results are possible with the interface strategy (Supplementary Fig. 19a). By contrast, hydrogels (12 mm × 8 mm × 500 μm) with the same chemical formulations but applied without a primer, fail to provide device/tissue adhesion and allow for significant movements of the devices under otherwise identical conditions (second row in Fig. 3d). Two out of three devices in this experiment emerge entirely from the body within 3 days post-surgery through regions between the sutures. Analysis in Fig. 3e, along with Supplementary Fig. 19b and Supplementary Note 9, indicate that the locations of devices integrated with the BTIM remain unchangeable within experimental uncertainties for up to two months, for both encapsulation and interface strategies (Fig. 3f and Supplementary Video 2). Furthermore, the devices remain functional throughout (Fig. 3g and Supplementary Video 3). By contrast, the displacements of the one device with a non-adhesive hydrogel that remained in the body of the animal are ~ 6 mm from day 2 to day 5 and ~ 17 mm from day 5 to day 8.

These materials and devices also present no measurable influence on the natural behaviors of the animals or their health status. Results of motion tracking (5 min in a rectangular arena) of mice implanted on day 10 and day 30 post-surgery are similar to those of control animals without implants (Supplementary Fig. 20). The surgical wounds heal completely with regrown fur after several weeks (Fig. 3h and Supplementary Fig. 21). Histological analysis of the dorsal subcutaneous area of BTIM-implanted mice four weeks post-surgery provides evidence of negligible influence on the morphology of the tissues and cells (Fig. 3i-k). Statistical analyses show that the adipocyte cell size, myofiber cell size, and skin thickness are 1030 ± 150 μm^2, 1120 ± 140 μm^2, and 580 ± 130 μm, respectively, in the BTIM group. These values in the sham group are 1120 ± 220 μm^2, 1140 ± 180 μm^2, and 590 ± 120 μm, respectively.

Wireless optogenetic electronic platforms

Similar adhesive strategies are effective for devices that support optogenetic stimulation[21,29-31] in the deep brain. Fig. 4a shows a lightweight, thin, battery-free, and wireless device for this application. This system includes a filamentary probe that supports

a microscale ILED (μ-ILED; wavelength: 590 nm) at its tip end for insertion into a targeted region of the brain. The back end consists of a receiver coil that supports wireless inductive power harvesting, along with associated interconnects and components. This part of the system mounts on the skull firmly by the BTIM using the encapsulating strategy (detailed surgical procedures in Supplementary Fig. 22). Fig. 4b and Supplementary Video 4-5 highlight the stable positioning of the receiver coils and interconnects by the BTIM (thickness: 300 μm). Fig. 4c shows a combined image that overlays magnetic resonance imaging (MRI) slices with MicroCT reconstructions two weeks post-surgery, to highlight the positions of the device and the BTIM. The devices enable deep tissue optogenetic stimulation with lifetimes of at least 2 weeks (insets of Fig. 4c and Supplementary Video 6). Furthermore, for transcranial optogenetic experiments, similar evaluations of the device positions by MicroCT prove that the BTIM-encapsulated device remains in its original location throughout the period of study, within experimental uncertainties (Fig. 4d, Supplementary Note 9 and Extended Data Fig. 5), compared with non-adhesive devices. Stabilization of the μ-ILED provided by BTIM greatly increases the rate of success in such experiments. Immunostaining of glial cell markers (glial fibrillary acidic protein, GFAP; ionized calcium binding adaptor molecule 1, IBA1) determines the activation of astrocytes and microglial cells in response to BTIM (thickness: ~ 500 μm) and sham surgery (Fig. 4e-f and Extended Data Fig. 6a-c). For GFAP, the astrocyte area percentages are 22 ± 4 % for the sham group and 25 ± 3 % for the BTIM group. For IBA1, the microglia area percentages are 14 ± 8 % for the sham group and 13 ± 3 % for the BTIM group. The negligible difference evidences the biocompatibility of the BTIM with brain tissue. Furthermore, the results clearly have potential for use in mice genetically modified for optogenetics studies, with robust adhesion to cerebrum (Extended Data Fig. 6d-e and Supplementary Video 7).

Bioresorbable optical filters

In addition, the BTIM can be used to secure bioresorbable optical filters[32] on the exposed surface of the brain for at least two weeks (Fig. 4g-h and Supplementary Fig. 23), providing a potential means for spectroscopic characterization of physiological status and neural activity[32]. The filter (Supplementary Fig. 24) consists of 15 pairs of SiO_x and SiN_y layers (thickness: 54 and 85 nm, respectively) on a film of PLGA (thickness: 10 μm). The transmission spectrum reveals that the device encapsulated with the BTIM can effectively block excitation light (wavelength: 450 – 520 nm) and transmit emission light (wavelength: 520 – 900 nm), as shown in Fig. 4i. This transmission window is relevant to applications that characterize neural calcium transients using genetically encoded fluorescent calcium indicators[32-35].

Interconnects/cables with adhesive conduits

Other classes of devices include wireless bioelectronic systems with sensors or actuators that lie in deep tissues at locations of interest[30,36]. In such cases, interconnects/cables often span between these components and functional modules that reside in subcutaneous tissues, typically for power harvesting, wireless communication, and/or analog-digital conversion. The schematic illustration in Fig. 4j shows how the encapsulation strategy can yield an adhesive ‘tunnel’, or conduit, in a soft, deformable encapsulation structure of

BTIM that bonds to the surrounding tissues but not to the enclosed interconnects/cables. The interconnect/cable surfaces exclude the APTES functionalization. Such approaches effectively confine the motion of the interconnects/cables to eliminate adverse effects on the system and the adjacent tissues. The result allows for flexible and reliable electrical connections under a variety of working conditions (Fig. 4k-l and Supplementary Video 8).

Wireless electrical cardiac pacing

Stable electrical interfaces for measurements and stimulation are essential in many biological applications, especially for the cardiac system. The inset in Fig. 5a highlights a thin, flexible, miniaturized, battery-free, wireless, leadless cardiac pacemaker (40 mm × 10 mm × 200 μm) that includes a pair of pacing electrodes, along with a rectangular PLGA/PU frame (8 mm × 8 mm; detailed information in Supplementary Fig. 25), designed to attach to the anterior epicardial surface of the ventricles. The BTIM coating establishes conformal contact between the electrodes and the myocardium, as shown in Fig. 5a and Supplementary Video 9. This scheme yields a gentle, conductive, stable interface between the device and the beating heart (first panel in Fig. 5b; detailed surgical procedures in Supplementary Fig. 26a-f), without tissue damage or bleeding during suturing (second panel in Fig. 5b). Composite images (first panel in Fig. 5c) highlight attachment of the electrodes to the heart one week post-surgery. The magnified image at the second panel of Fig. 5c highlights the position within the rat anatomy. Manual mechanical tests indicate strong adhesion (Fig. 5d, Supplementary Fig. 26g-i and Supplementary Video 10-11) across 10 days post-surgery.

Histological evaluations of fibrotic tissues serve as a basis for comparing pacemakers secured with sutures (first panel) to those with the BTIM (second panel), as in Fig. 5e. Although the levels of fibrosis in the two cases are similar, large perforations in the cardiac muscle appear with surrounding fibrotic tissues induced by the suturing process, potentially resulting in compromised mechanical contraction of the myocardium and in life-threatening arrhythmias during implantation procedures and after surgery. The differences are evident in a double-blinded clinical-scoring system highlighted in Fig. 5f, which defines the amount of disorganized connective tissue on top of the myocardium on a scale of 0 – 5. The clinical score for suturing is 2.8 ± 0.3 (P = 0.0215 versus control group), consistent with dense scar tissue that requires sharp instrumentation to disrupt. The score for the BTIM is 1.8 ± 0.6 (P = 0.4334 versus control group), corresponding to a relatively small amount of scar tissue that can be disrupted with blunt instruments. As shown in Fig. 5g, Masson’s trichrome staining of tissue cross-section four weeks post-surgery indicates volume fractions of interstitial space (I), myocytes (M), and collagenous tissue (Ct) that are 10 ± 6%, 69 ± 12%, and 21 ± 9%, respectively. For the case of sutures, these same quantities are 10 ± 5%, 78 ± 7%, and 12 ± 7% and in the control group 6 ± 4%, 85 ± 7%, and 9 ± 4%. Compared with the control group, the BTIM induces no significant differences in myocardial volume fraction, which is consistent with an absence of myocardial damage.

Differences in biocompatibility at the electrode/tissue interface are largely responsible for differences between functional lifetimes of pacemakers implanted with the BTIM and with sutures. Studies to compare these two options involve daily pacing trials under light sedation with electrocardiogram (ECG) recordings (Supplementary Note 10 and Supplementary Fig.

27). Fig. 5h compares the threshold voltages for pacing. Values for the sutured devices increase rapidly and reach a failure criterion (0.7 V) on day 6 post-surgery (the one of the two devices fails to pace within 1 day). Failure results are mainly due to an increased level of disorganized non-conductive connective tissue that develops at the surface of the myocardium, as evaluated by the clinical score in Fig. 5f. By comparison, devices mounted with the BTIM allow pacing up to day 8 post-surgery, with only slight increases in threshold voltage (0.04 V on day 1 – 0.10 V on day 8). Fig. 5i presents representative ECG traces recorded during rapid ventricular pacing in different rhythms on day 0, at ~ 400, 600, and 1000 bpm (Supplementary Video 12). Fig. 5j similarly shows ECG traces obtained throughout the pacing period of 8 days post-surgery, with a minimal increase in threshold voltage (full pacing details shown in Supplementary Fig. 28).

Electrical spatiotemporal mapping

The same adhesive strategy can be used for mapping of cardiac electrophysiology using flexible electrode arrays, without the limitations associated with previously described schemes[37,38]. Fig. 6a presents a device designed for this purpose with 64 electrodes (multielectrode array, MEA; 8 columns, 8 rows; parylene/Cr/Au/parylene: 4/0.01/0.3/4 μm; 500 μm × 500 μm for each electrode; 13 mm × 13 mm in total). Fig. 6b-c provide schematic illustrations and images of integration strategies based on the BTIM encapsulation (Fig. 6b) and interface (Fig. 6c) methods (thickness: 500 μm) on Langendorff-perfused rabbit hearts in a constant pressure system *ex vivo*. High quality normalized electrograms of sinus rhythms from a representative electrode associated with the these methods verify the ability to capture electrophysiological signals (ECG traces measured from each electrode appear in Supplementary Fig. 29). Images in Fig. 6d show the MEA configuration on the epicardial surface (first panel: interfacial layer; second panel: encapsulating coating). The photographs in Fig. 6e highlight stable adhesion after 8 h of testing in the Langendorff perfusion system, including manual evaluations of the robustness of the bonding. The adhesion strength supports the gravitational forces associated with the rabbit heart (weight: ~ 8 g) with no significant delamination.

The amplitudes of electrograms recorded with devices after integration with these methods, as shown in Fig. 6f-g, are similar to those collected with devices held by capillary forces associated with the presence of biofluids. Specifically, data collected before and after applying the encapsulation method are 4.1 ± 1.4 mV and 3.5 ± 0.6 mV, respectively; those with the interfacial method are 1.8 ± 0.5 mV and 1.3 ± 0.6 mV, respectively. The time coincidence of simultaneous recordings of electrograms and optical action potentials (OAP) indicates consistency between these two signals, showing the effectiveness of the BTIM for cardiac mapping applications (Supplementary Fig. 30). Strong spatial correlations of time coincident optical (first panel; captured at 100 × 100 pixels) and electrical activation maps (second panel; captured at 8 × 8 electrode array; lineshape fitting) recorded with MEAs attached by the encapsulation (Fig. 6h) and interface (Fig. 6i) methods provide further evidence of proper operation of MEAs with the BTIM. Such an integrated system can also accurately map ventricular fibrillation, as shown in Extended Data Fig. 7 and Supplementary Video 13.

Conclusions and outlook

The results described here span topics in material formulations, integration schemes, and *in vivo* evaluations of functional, soft adhesive materials for bioelectronic/tissue interfaces. Systematic studies of the chemical, mechanical, electrical, and optical properties define the key materials science aspects of this system. Comprehensive evaluations in animal models illustrate all of the essential features as well as the applicability to a diverse collection of bioelectronics devices across multiple organs. In all cases, the BTIM softly joins these electronic/optoelectronic devices to moving tissues as functional interfaces for sensing and stimulation, without adverse immune responses or device dislocation. These materials strategies have immediate potential for applications in biological research on animal models, and they offer promise for eventual use in humans. The concepts may also form a starting point for further developments of advanced biotic-abiotic interfaces to support multifunctional diagnosis and treatment in both acute and chronic medical applications. Additional improvements in the interface chemistry may allow for robust stable bonding between bioelectronics systems and tissue surfaces throughout the time course of chronic diseases and disorders, where the timescales may extend from many months to years (Discussions on potential failure modes and solutions to long-term material and device reliability appear in Supplementary Note 11). Other possibilities are in the development of materials that support the bidirectional transport of drugs or biochemical species, to complement capabilities supported by electrical and/or optical interfaces.

Methods

Materials

The starting materials included polyethylene glycol (M_w: 35 kDa), 2-hydroxy-1-[4-(2-hydroxyethoxy) phenyl]-2-methyl-1-propanone (Irgacure D-2959), lactide, triethylamine, acryloyl chloride, Tin(II) 2-ethylhexanoate [$Sn(Oct)_2$], dichloromethane (anhydrous), toluene (anhydrous), potassium carbonate (K_2CO_3), calcium chloride ($CaCl_2$) and magnesium sulfate ($MgSO_4$) purchased from Sigma-Aldrich (MO, USA), ethyl ether (anhydrous) purchased from Thermo Fisher Scientific (MA, USA), micro-filtered and lyophilized sodium alginate (MVG GRGDSP-coupled; high G ratio; high M_w) purchased from NovaMatrix (Dupont, DE, USA), high purity chitosan (99% degree of deacetylation; M_w: 100 kDa), as primers for tissues, purchased from Sigma-Aldrich (MO, USA), and 1-ethyl-3-(3-dimethylaminopropyl) carbodiimide (EDC) and sulfated N-hydroxysuccinimide (Sulfo-NHS), as coupling reagents for tissue and device primers, purchased from Thermo Fisher Scientific (MA, USA). The solvents included ultrapure distilled water, phosphate-buffered saline (PBS; pH 7.4), and 2-(N-morpholino)ethanesulfonic acid (MES; pH 5.0) purchased from Thermo Fisher Scientific (MA, USA). All chemicals were used as received. Tissues and organs for bench studies were purchased from Animal Biotech Industries (ABI; PA, USA) and were cleaned with soap and water before adhesion measurements.

Synthesis

Synthesis of polyethylene glycol-lactide (PEG-LA) bioresorbable copolymer— The α- and ω-hydroxyl end groups of commercial PEG served as ring-opening reagents

to initiate the polymerization of lactide to form copolymers. The amount of lactide units, defined by the number x (x = 2, 4 and 10) in PEG-xLA, determines the degradation rate of the material, where x refers to the theoretical number-averaged degree of polymerization of lactide on each end of the PEG. Dissolving PEG (1 eq., 54 g) in 170 mL anhydrous toluene mixed with lactide (2 eq., 0.358 g) and [$Sn(Oct)_2$] (0.1 eq., 0.062 g), followed by purging with nitrogen and then heating at 110 °C for 24 h under constant stirring formed the PEG-2LA. Precipitating the PEG-2LA in anhydrous ethyl ether, followed by filtering and drying under vacuum for 24 h at room temperature, yielded dry PEG-2LA with hydroxyl end groups. Adding different amounts of lactide monomers during the reaction formed corresponding PEG-4LA and PEG-10LA terminated with hydroxyl groups.

Synthesis of PEG-xLA-DA macromere—The addition of acrylate groups to hydroxyl-terminated PEG-xLA yielded polymerizable macromers, via the following steps[39]. PEG-xLA (1 eq., 50 g) and triethylamine (4 eq., 0.83 mL) were dissolved in 500 mL anhydrous dichloromethane and then cooled to 0 °C in an ice bath. Acryloyl chloride (4 eq., 0.5 mL) was added dropwise under constant stirring, followed by reaction for 12 h at 0 °C and 12 h at room temperature, respectively. The PEG-xLA-DA solution was washed with 5 wt% K_2CO_3 solution, dried with $MgSO_4$, and precipitated in ethyl ether. Further purification of PEG-xLA-DA involved two cycles of dissolution and precipitation in dichloromethane and ethyl ether, respectively. Drying under vacuum conditions for 24 h at room temperature completed the synthesis of the polymerizable macromers. The synthesized materials were characterized by AVANCE III-500 MHz solution NMR spectrometer with DCH cryoprobe (Bruker, MA, USA) and MALDI-TOF (Bruker, MA, USA). ^{1}H NMR data were collected by TopSpin 3.6.2 (Bruker, MA, USA) and analyzed by Mnova 8.1.4 (Bruker, MA, USA). Mass spectrum were collected by flexAnyalysis 3.4 (Bruker, MA, USA) and polytool 2.0 (Bruker, MA, USA).

Synthesis of the BTIM—Synthesis began with dissolving PEG-LA-DA (40.0 wt%), Irgacure D-2959 (0.4 wt%), and $CaCl_2$ (0.5 wt%) in ultrapure water to form solution A (pH 7). Dissolving sodium alginate (5.0 wt%) in ultrapure water formed solution B (pH 7). Bubbling nitrogen gas (N_2) into solution A and B for 10 min followed by degassing removed most of the dissolved oxygen (O_2). Mixing solution A and B at a ratio of 1:1, followed by exposure under ultraviolet light (UV; wavelength: 365 nm; density: 20 mW/cm^2) for 3 min, cured the bioadhesives, in a standard process used throughout the experiments and studies presented here.

The primers utilized carbodiimide reagents (EDC, 0.5 wt%; Sulfo-NHS, 0.5 wt%) in MES buffer (pH 5). Certain steps in the synthesis followed protocols published in a previous study[15]. The process began with dissolving chitosan (2.0 wt%) in MES buffer (pH 5) followed by the addition of carbodiimide reagents (EDC, 0.5 wt%; Sulfo-NHS, 0.5 wt%).

Integration strategies

Encapsulating coating—The procedure began with placing the device on the tissue and then spreading primers on the surfaces of both. Introducing a mixture of solution A and B onto the device and adjacent areas of tissue and then exposing to UV completed the process.

Interfacial layer—The procedure began with treating the bottom surface of the device with UV-induced ozone to create surface hydroxyl groups, followed by soaking in (3-aminopropyl)triethoxysilane (APTES; 5 vol% in the mixture of ethyl alcohol and water at a ratio of 1:1) for 30 min to form amine termination. After APTES functionalization (detailed information in Supplementary Note 3), the device surfaces were immediately rinsed by ethanol, IPA, and DI water in sequence, each for 2 min, followed by immersion in DI water for 5 min, to remove the residues of ethyl alcohol and APTES. Functionalization proof through ToF-SIMS analysis and measurement of APTES thickness through spectroscopic ellipsometry utilized WinCadence 5.4.0.5 (Physical Electronics, MN, USA) and EASE 3.01D (J.A. Woollam, NE, USA), respectively. The Applying primers and precursor mixtures, sequentially, at the interface between the tissue and the device, followed by UV exposure, formed a strongly bonded interface. For opaque devices, adding transparent materials, such as PLGA or parylene, around the perimeter (extending length: ~ 2 mm), yielded sites for interfacial bonding.

Supporting matrix—The techniques of compressive buckling formed the three-dimensional electronic structures presented here. The strategy began with casting the precursor mixture onto the structures, followed by UV exposure, to yield a free-standing component with BTIM as a matrix supporting the three-dimensional electronic structure inside. Applying primers and additional precursor mixtures to the surfaces of this system and the tissue, followed by manual placement and UV curing, completed the integration.

Characterization of the BTIM

Adhesion energy—Characterization involved peeling adhering specimens (50 mm × 5 mm × 2 mm) from the tissue surfaces and encapsulation/substrate materials of the devices (50 mm × 5 mm; various thicknesses for different materials). Films of PLA (thickness: 50 μm) bonded to the specimens and the tissue samples minimized the contribution of elastic energy dissipation to the test results. The peeling rate was 20 mm/min. Two times the value of the plateau force divided by the width of the specimen yielded the adhesion energy. Peeling tests and the following tensile tests were performed by MTS Sintech 20G (MTS, MN, USA) and the data were collected by its recording software.

Mechanical properties—Tensile tests used unnotched and notched specimens (50 mm × 5 mm × 2 mm). Notched samples included a 25-mm-long crack from one edge to the middle, perpendicular to the stretching direction. The tensile rate was 15 mm/min. The slopes of stress-strain curves in the elastic zone of unnotched specimens defined Young's moduli. The area under the stress/strain curves for unnotched specimens up to the strain at initial crack propagation defined the toughness[40].

Rheology—The shear storage modulus served as a metric for characterizing the crosslinking density as a function of UV exposure time. Measurements used a modular compact rheometer (MCR302; Anton Parr GmbH, Graz, Austria) with a 25-mm-diameter cone plate (CP25) at an amplitude and angular frequency of 5% and 1 Hz, respectively. UV exposure began at 120 s and ended at 300 s. Data was collected using the RheoCompass software (Anton Paar GmbH, Graz, Austria).

Surface roughness—Analysis of surface roughness began with casting and curing a layer of BTIM on a sample of porcine skin without the use of primers. Carefully peeling the BTIM away from the porcine skin enabled measurements of the roughness of its interfacial surface. Scanning an area of 1.5 mm × 1.5 mm using a laser confocal microscope (LEXT OLS5000; Olympus Corporation, Tokyo, Japan) revealed the surface morphology and height distribution.

Transmittance—A UV/Vis/NIR spectrophotometer (LAMBDA 1050; Perkin Elmer, MA, USA) defined the transmittance of specimens (25 mm × 25 mm × 2 mm) for wavelengths between 200 to 1000 nm. Data was collected using UV WinLab software (LAMBDA 1050; Perkin Elmer, MA, USA).

Biodegradable behaviors—Evaluations involved gravimetric analysis, rheology, and CyroSEM imaging. Soaking BTIM specimens in PBS (pH 7.4, 37 °C) for a certain number of days, immersing these specimens in ultrapure water for 12 h to remove residual ions, and lyophilization (Labconco, MO, USA), enabled evaluation of the dried weights. The ratios of the dried weights to the original ones yielded the percentages of the remaining material, as a process of gravimetric analysis. Rheological measurements (MCR302; Anton Parr GmbH, Graz, Austria) from 0.1 to 100 Hz revealed changes of crosslinking density in specimens (diameter: 25 mm; thickness: 2 mm) at various times during degradation. CryoSEM imaging defined the corresponding changes in the microstructure. The process began with flash-freezing specimens by liquid ethane. A cryogenic transfer system (VCT100; Leica Camera AG, Wetzlar, Germany) shuttled the specimens in a vacuum coater (ACE600; Leica Camera AG, Wetzlar, Germany) to cool them to −120 °C. After freeze-etching for 5 min at −105 °C, depositing 7-nm-thick platinum (Pt) on the surfaces of the specimens minimized charging for imaging in a CyroSEM (S4800-II cFEG SEM; Hitachi, Tokyo, Japan) at −135 °C and a beam voltage of 5 kV.

Simulations

Commercial software (ABAQUS Analysis User's Manual 2010, V6.10) was used to study the stress distributions near the surfaces of biological tissues integrated with devices under typical loads, such as bending-over and side-bending. The effects of the BTIM thickness (500 and 1000 μm) and the device modulus (2 MPa and 2 GPa) were studied thoroughly. The coefficients of friction at the tissue/device interface and the tissue/BTIM interfaces were 0.15 and 0.05, respectively[41,42]. The elastic modulus and Poisson's ratio were E_{tissue} = 50 kPa and ν_{tissue}= 0.5 for tissue, E_{BTIM}= 30 kPa and ν_{BTIM}= 0.5 for BTIM.

Commercial software (COMSOL 5.2a) in the electric current module (2D model; AD/DC Module User's Guide) was used to study the influence of BTIM conductivity on bioelectronics performance for electrical stimulation and biopotential sensing. In both cases, the thickness, length, and conductivity for biological tissues (myocardium) were 2 mm, 8 mm, and 0.16 S/m, respectively. These parameters for BTIM were 0.5 mm, 8 mm, and in the range between 0.001 to 100 S/m. For electrical stimulation, the parameters were chosen to be close to those in the applications of wireless pacemakers in a rat model. The pair of metal electrodes (material: molybdenum; length: 1 mm; thickness: 50 μm; spacing: 3 mm)

possessed a conductivity of 1.9×10^7 S/m. A voltage at a value of 3 V was given to the electrodes for cardiac pacing. For biopotential sensing, the parameters were close to those in the applications of ultra-thin MEA on the Langendorff-perfused rabbit heart. The eight electrodes of the MEA (material: gold; length: 500 μm; thickness: 300 nm; spacing: 1 mm) had a conductivity of 4.5×10^7 S/m/. A fixed potential (linear form; 1 V on the left endpoint and 0 on the right endpoint) was given on the top surface of the myocardium layer. The internal resistance of the measurement setup is considered as ~ 1 – 100 MΩ. Convergence test of the mesh size had been performed to ensure accuracy. The total number of elements in the models is approximately ~700,000.

Integration process for device arrays and 3D multilayer, electrode-embedded, and electrode-exposed electronic systems

Device arrays and multilayer structures—Individually casting primers and precursor mixtures onto bare silicon chips coated with a layer of fluorescent acrylic paint and then placing them onto a sample of porcine skin, followed by UV exposure, yielded an array of 19 components in the shape of ‘NU’. Repeating this process yielded a three-layer system.

3D electrode-embedded electronic systems—Fabrication began with spin-coating a layer of polyimide (PI, thickness: 3 μm) on a silicon wafer coated with a layer of polymethyl methacrylate (PMMA). Depositing a bilayer of Cr/Au (thickness: 10/100 nm) by electron beam evaporation, followed by photolithography (AZ5214; thickness: ~ 1.4 μm) and wet etching defined a pattern of electrodes. Eliminating the PMMA by immersion in acetone for 3 h allowed the transfer of the 2D structure from the silicon wafer to a water-soluble tape. Deposition of SiO_2 (thickness: 100 nm) through a stencil mask (PI; thickness: ~ 10 μm) by sputtering (AJA International Inc., MA, USA) on the backside of the PI defined bonding sites. Exposing a pre-stretched silicone elastomer and the SiO_2 surface on the PI to UV ozone formed hydroxyl termination. Attaching the PI, as a 2D precursor, onto the stretched elastomer, followed by heating (60 °C, 15 min) and releasing the pre-strain, yielded the desired 3D configuration. Applying precursor mixtures to fully embed the 3D structure, followed by UV exposure and removal from the substrate, yielded a 3D free-standing electrode-embedded electronic system. Spreading primers and extra precursor mixtures on the surfaces of the device and the biological tissues enabled strong bonding. Impedance measurements over frequencies between 1 to 10^5 Hz utilized a commercial potentiometer (Autolab PGSTAT128N; Metrohm AG, Herisau, Switzerland) with an Ag/AgCl reference. Data were collected by AutoLab NOVA v2.1.4 (Metrohm AG, Herisau, Switzerland).

3D electrode-exposed electronic systems—Fabrication began with patterning a layer of PLA (thickness: ~ 50 μm) by laser cutting (ProtoLaser R; LPKF Laser & Electronics, Garbsen, Germany). Depositing Cr/Au (thickness: 5/50 nm) through a stencil mask (PI; thickness: ~ 10 μm) by electron beam evaporation (AJA International Inc., MA, USA) defined the pattern of electrodes. Deposition of SiO_2 (thickness: 100 nm) through another stencil mask (PI; thickness: ~ 10 μm) by sputtering (AJA International Inc., MA, USA) on the backside of the PLA defined bonding sites. Exposing a pre-stretched silicone elastomer and the SiO_2 surface on the PLA to UV ozone formed hydroxyl termination. Attaching PLA, as a 2D precursor, onto the stretched elastomer, followed by heating (60 °C, 15 min) and

releasing the pre-strain, yielded the desired 3D configuration with exposed electrodes on the surface. Injecting precursor mixtures inside the 3D structure, followed by UV exposure, created an electrode-exposed electronic system. The precursor mixtures filled the interior space due to capillary interaction. Removing this system from the silicone elastomer, coating it with primers and precursor mixtures, and then exposing to UV, allowed for integration with biological tissues.

In vitro cytocompatibility

A mouse cell line (ATCC® CCL-1™, L-929; VA, USA) was used for characterizing cell migration into the BTIM. A mixture of Minimum Essential Medium Eagle (EMEM; ATCC® 30-2003™; VA, USA), 10 vol% fetal bovine serum (FBS; Thermo Fisher Scientific, MA, USA), and 1 vol % Penicillin-Streptomycin (Pen-Strep; Thermo Fisher Scientific, MA, USA) served as the cell culture medium. The cells were maintained and cultured in a 6-well cell culture insert (Thermo Fisher Scientific, MA, USA). Placing a matrix of the BTIM (diameter: 2 cm; thickness: 500 μm) with platelet-derived growth factor (PDGF; concentration: 16 ng/mL; Sigma-Aldrich, MO, USA) into the medium, which was replaced every two days, led to ingrowth. After one week, immersing the specimen in formaldehyde (4 vol% in PBS; PBS: 0.1 M, pH 7.4; Sigma-Aldrich, MO, USA) at room temperature for 30 min fixed the adhesive matrix. Rinsing with PBS (0.1 M, pH 7.4) 3 times removed the formaldehyde. Incubating the adhesive matrix in Triton X-100 (0.1 vol% in PBS; PBS: 0.1 M, pH 7.4; Sigma-Aldrich, MO, USA) at room temperature for 5 min permeabilized the cell membrane. The adhesive matrix was then blocked with BSA (1 vol% in PBS; PBS: 0.1 M, pH 7.4) at room temperature for 1 h. After removing the BSA by rinsing with PBS (0.1 M, pH 7.4) 3 times, staining the adhesive matrix with F-actin maker rhodamine-phalloidin (Thermo Fisher Scientific, MA, USA) at room temperature for 40 min, followed by counterstaining with 4', 6-diamidino-2-phenylindole (DAPI; Thermo Fisher Scientific, MA, USA) for 10 min, enabled imaging through Leica SP8 confocal microscope (Leica Camera AG, Wetzlar, Germany) and Hitachi SU8030 SEM (Hitachi, Tokyo, Japan) to observe the cell morphology in the adhesive matrix. Before SEM imaging, the cells in the matrix were fixed by glutaraldehyde (2.5 vol% in PBS; PBS: 0.1 M, pH 7.4) at 4 °C for 2 h. The matrix was dehydrated in graded alcohol of 30%, 50%, 60%, 70%, 80%, 90%, 95%, and 100%, and finally was dried with CO_2 in a critical point dryer. The specimen was sputter-coated with osmium (Os; thickness: ~ 10 nm) before observation. Images were captured and data were analyzed by Gen5 software (BioTek Instruments, VT, USA).

Sterile processes for animal studies

Micro-filtered and lyophilized sodium alginate and high purity chitosan were dissolved in ultrapure water (0.5 wt%), sterile filtered (220-nm-diameter membrane pores), frozen at −20 °C for 3 h, and then lyophilized (Labconco, MO, USA) for 6 h. After lyophilization, the sterile alginate and chitosan were stored at - 20 °C before usage. The other chemicals, including PEG-xLA-DA, $CaCl_2$, Irgacure D-2959, EDC, and Sulfo-NHS were sterilized by filtering immediately before use. The synthesis process was performed in a tissue culture hood, and the precursor solutions were stored in 3-mL-volume syringes. External equipment, involving surgical tools, adaptors, and UV lamps, were wiped with cloths soaked in 75%

ethanol. All components and devices were sterilized using the ethylene oxide (EtO) gas method.

Animals for *in vivo* characterizations

Animals procedures were performed according to protocols approved by the Institutional Animal Care and Use Committee (IACUC) at Northwestern University and The George Washington University, and conformed to the Guide for the Care and Use of Laboratory Animals. For the studies on dorsal subcutaneous tissues and brains, young adult male and female C57BL/6 mice (postnatal days: 60 – 80; weight: ~ 20 g) were used. Mice were maintained at ~ 25 °C and humidity ranged of 30 % to 70 %, on a standard 12-h light/12-h dark cycle (lights on at 6:00 or 7:00 AM) and fed ad libitum. Mice were group-housed (two to four per cage) prior to surgery, after which mice were individually housed in a climate-controlled vivarium. Approximately equal numbers of males and females were used. For cardiac studies, Sprague Dawley or Long Evans adult rats of both sexes (weight: 300 – 600 g) were used. Rats are housed at 72 °F and a humidity between 30 – 70 % on a standard 12-h light/12-h dark cycle. For ECG mapping, female New Zealand white rabbits (3-6 months old) were used for the study. Rabbits are housed at 72 °F and a humidity between 30-70% on a standard 12-h light/12-h dark cycle.

Surgical procedures for wireless devices for dorsal subcutaneous implantation

The devices consisted of wireless, battery-free miniaturized optoelectronic systems based on NFC technology (~ 10 mm × 8 mm × 1 mm - at the thickest regions). Mice were anesthetized with isoflurane (induction value: 3 %; maintenance value: 1.5 – 2 %), received ketoprofen (5 mg/kg, i.p.) for analgesia, and were placed on a small animal stereotaxic frame (David Kopf Instruments, CA, USA) for the surgery. Puralube vet ointment (Dechra Veterinary Products, KS, USA) was applied to cover the eyes during this procedure. A 1-cm-long incision was made over the shaved back to expose the subcutaneous tissues. The device was then placed on the subcutaneous tissue, followed by a PDMS mold to control the spread of the liquid precursor mixture. UV exposure followed the application of primers and precursors into this mold, and directly onto the device and adjacent regions of the tissue. After implantation, nylon 6-0 monofilament (Ethicon Inc., NJ, USA) sutures were applied to close the wounds, with standard post-surgical recovery procedures.

Evaluations of adhesive bonds for dorsal subcutaneous devices

Positional stability by MicroCT analysis—MicroCT imaging performed on different post-surgical days determined the positional stability of these devices. Mice were anesthetized in an induction chamber with 3 % isoflurane in oxygen and transferred to a dedicated imaging bed with isoflurane delivered via a nosecone at 1 – 2 %. The mouse was placed in the prone position in a dedicated chamber with the head immobilized using ear and tooth bars. Respiratory signals were tracked using a digital monitoring system (Mediso-USA, MA, USA). Images were acquired at 2.17 magnification, using 33 μm focal spot, 1 × 1 binning, with 720 projection views over a full circle and a 300 ms exposure time, using 70 kV_p. The projection data were reconstructed with a voxel size of 68 μm using filtered (Butterworth filter) back-projection software from Mediso. The reconstructed data

were visualized in Amira 6.7 (FEI, TX, USA). MicroCT images were manually registered, since artifacts caused by the device precluded automatic image registration.

Measurement of device translation—All analysis was performed using Amira 6.2 software. MicroCT scans, which were modified using a non-local means filter, segmented the device at each timepoint (day 2, 5, and 8 post-surgery) with a combination of thresholding and manual segmentation. Cropping the skeleton of the mouse, segmented using a threshold of 700 Hounsfield units (HU), resulted in a region of interest containing only L3, L4, L5. The vertebral segments from the second and third timepoints were automatically registered to the vertebral segment from the first timepoint using Normalized Mutual Information. Each vertebral transform was copied to its corresponding device so that all devices were registered to the vertebrae from the first timepoint. The device regions of interest were binarized using an automated adaptive thresholding tool, and the centroid of each device was noted.

Evaluation of functionality of dorsal subcutaneous devices

Optical characterization—A commercial RF system (Neurolux, IL, USA) wirelessly delivered power to activate the devices. Visual observation of light from the ILED enabled inspection for device functionality every two days. The mice with implants freely roamed within an enclosed cage encircled by a loop antenna connected to a laptop with a software control interface to a power distribution control box and an antenna tuner box (Neurolux, IL, USA). The cage equipped with a wireless system allowed mice to move freely without tethers. A cellphone with NFC capability placed close (<1 cm) to the dorsal subcutaneous tissues provided an alternative means to initiate the illumination. Evaluations were performed for two months until the devices ceased to function.

Evaluations of biocompatibility for BTIM-encapsulated dorsal subcutaneous devices

Locomotion characterization—The tests involved studies of locomotor activity of mice with and without implanted devices (experimental and control groups, respectively). The trials began with placing mice one at a time in the center of a plastic chamber (48 cm × 48 cm × 40 cm) in a dimly lit room. Animals explored the arena for 15 min, with video (frame rate: 30 fps) capture of their behavior during the final 5 min by Raspberry Pi Camera v2 (Raspberry Pi Foundation, Cambridge, UK). Comparison of the trajectories of locomotor behaviors and statistical evaluations[43] of the distance traveled in each session relied on monitoring the body center of the animal using Toxtrac v2.90[44].

Immunofluorescence staining—Animals implanted with the BTIM were sacrificed on week 1, 3, 5, and 7 post-surgery. 10-μm-thick dorsal epidermal tissue sections were collected by CMI1850UV Cryostat (Leica Camera, Wetzlar, Germany). Rinsing tissue sections with PBS (0.1 M) at room temperature for 30 min removed the optimum cutting temperature (OCT) compound. Fixing with formaldehyde (4 vol% in PBS; PBS: 0.1 M, pH 7.4; Sigma-Aldrich, MO, USA) at room temperature for 30 min, followed by rinsing with PBS (0.1 M, pH 7.4) 3 times removed formaldehyde. Incubating with Triton X-100 (0.1 vol% in PBS; PBS: 0.1 M, pH 7.4; Sigma-Aldrich, MO, USA) at room temperature for 10 min permeabilized the cell membrane. After 3 cycles of rinsing with PBS (0.1 M, pH 7.4), the

tissue sections were blocked with BSA (1 vol% in PBS; PBS: 0.1 M, pH 7.4) at room temperature for 1 h. Two kinds of primary antibodies for macrophage (CD68+, 0.5 % and CD163+, 0.5 %; Abcam, Cambridge, UK) were utilized to incubate the tissue sections at 4 °C for 12 h. After three cycles of rinsing with PBS (0.01 M, pH 7.4), the tissue sections were further incubated with the secondary antibodies (goat anti-mouse 488 and goat anti-rabbit 568; Abcam, Cambridge, UK). Applying DAPI (Thermo Fisher Scientific, MA, USA) as a fluorescent stain, counterstained the cell nucleus. Micrographs were obtained with an SP8 confocal microscope (Leica Camera, Wetzlar, Germany).

Hematoxylin and eosin (H&E) staining—Mice were deeply anesthetized with isoflurane and transcardially perfused with 10% Neutral buffered formalin (NBF). Back tissue was post-fixed for 7 days prior to processing and sectioning. The standard protocols for H&E staining were followed. Four micron-thick issue sections adhered to slides were dewaxed and cleared with xylene, hydrated through incubation in a series of decreasing concentrations of alcohols (100 – 70%), stained with filtered hematoxylin, treated with an alkaline solution, and counterstained with eosin. Subsequently, sections were dehydrated in several changes of alcohol, cleared, and coverslipped. Sections were imaged using an Olympus VS120 microscope (Olympus Corporation, Tokyo, Japan) in brightfield mode. Colored bright-field images of back tissue sections were automatically acquired and stitched by using an automated slide scanner and a 20x objective. Analysis was carried out in FIJI[43,45] using line and area measurement. The same analysis parameters were applied across all regions of interest.

Surgical procedures for wireless devices for deep brain optogenetics

The devices consisted of wireless optogenetic platforms based on NFC technology for untethered neuronal control and discrete spatiotemporal targeting of neural circuits. The constituent components included a penetrating probe with a microscale inorganic light-emitting diode (μ-ILED) at its tip end for insertion into the deep brain and a receiver coil for wireless power harvesting above the skull in the subcutaneous tissues. The fabrication process followed procedures described previously[2143,45]. Standard anesthesia and eye protection to mice proceeded as described above. A 5-mm-long incision made on the scalp exposed the skull allowed for drilling a hole for inserting the probe into the targeted brain regions. Coordinates for medial prefrontal cortex (mPFC) probe placement were + 2.0 mm (AP), + 0.4 mm (ML), and +1.5 mm (DV). The BTIM encapsulated the receiver coil and anchored the platform onto the skull. A 6-0 nylon monofilament (Ethicon Inc., NJ, USA) suture closed the wound after implantation.

Evaluation of adhesive bonds and device functionality of deep brain optoelectronics

Optical stimulation—Every two days, the implanted devices were wireless powered by a commercial RF system (NeuroLux, IL, USA) to activate the optical stimulation as an assessment of device functionality. The devices remained functional throughout the two-week period before sacrificing the animals. The optoelectronic systems remained firmly adhered to the skull throughout this time.

MicroCT and MRI imaging—Evaluations of device position after two weeks post-surgery were performed by MicroCT and MRI analysis. For MicroCT, see the procedures described previously. MRI was performed on a 9.4 T Bruker Biospec MRI system with a 30 cm bore, a 12 cm gradient insert, and an Autopac automated sample positioning system (Bruker Biospin, Billerica, MA). Respiratory signals were recorded using an MR-compatible physiologic monitoring system (SA Instruments, NY, USA). A warm water circulating system maintained body temperature. An actively decoupled, 4-channel phased array, receive-only radiofrequency coil designed specifically for the mouse brain (Bruker Biospin, MA, USA) was mounted on the bed. This assembly was centered inside a 72 mm quadrature volume coil in transmit-only mode (Bruker Biospin, Inc, MA, USA). Mice were imaged using an accelerated spin-echo sequence (Turbo Rapid Acquisition with Relaxation Enhancement, TurboRARE) oriented in axial, sagittal, and coronal directions. The following parameters were used: TR/TE = 1250 ms/21.3 ms, RARE factor 8, MTX = 256 x 256, FOV 3 x 3 cm, 7-13 slices of 0.75-1 mm thick (as needed for full brain coverage), flip back enabled, and 3 signal averages. The acquisition time was approximately 2 min per scan.

Evaluation of biocompatibility of BTIM-encapsulated deep brain optoelectronics

Tissue processing and immunohistochemistry—Mice with BTIM implantation were deeply anesthetized with isoflurane and transcardially perfused with 4% paraformaldehyde (PFA). Brain was extracted and post-fixed for 1-5 days prior to sectioning. 60-μm-thick sections were collected and incubated with rabbit anti-GFAP (1:1000; Abcam, Cambridge, United Kingdom), and rabbit anti-IBA1 (1:1000; Abcam, Cambridge, United Kingdom), as described in previous studies[46,47]. On the following day, tissues were rinsed three times with PBS, reacted with anti-rabbit Alexa Fluor 647 secondary antibody (1:500; Thermo Fisher Scientific, MA, USA) for 2 h at RT, rinsed again for three times in PBS. Sections were mounted on Superfrost Plus slides (Thermo Fisher Scientific, MA, USA), air dried, and cover slipped under glycerol:TBS (9:1) with Hoechst 33342 (2.5 μg/ml; Thermo Fisher Scientific, MA, USA). Whole sections were imaged with an Olympus VS120 slide scanning microscope (Olympus Corporation, Tokyo, Japan). Analysis was carried out in FIJI[32] using autothresholding and area measurement. The same analysis parameters were applied across all regions of interest.

Surgical procedures for bioresorbable optical filters for the brain

The optical filters consisted of bioresorbable multilayers of silicon dioxide (SiO_x; thickness of each layer: 54 nm) and silicon nitride (SiN_y; thickness of each layer: 85 nm) on a layer of PLGA (thickness: ~ 10 μm). The fabrication process followed those of a previous study[22]. Standard anesthesia and surgical procedures were similar to those described above. A 5-mm-long incision made on the scalp exposed the skull, to allow removal of a section (3 mm × 3 mm) for alignment and insertion of the filter onto targeted regions of the brain. The filter encapsulated with the BTIM touched the exposed cerebral area to modulate the transmission (wavelength: 520 – 900 nm) and reflection (wavelength: 450 – 520 nm) spectra for characterization of neural calcium transients based on GCaMP. A commercial fiber-optic spectrometer (Ocean Insight, FL, USA) measured the reflection spectrum of the optical filter.

Evaluation of adhesive conduits for interconnects/cables

These studies focused on interconnects/cables as electrical interfaces between devices for sensing/stimulating in deep tissues and receivers and other hardware for power supply, wireless communications, and other functions in subcutaneous tissues. The fabrication process began with photolithographic patterning of multilayer serpentine structures, consisting of parylene/Ti/Cu/Ti/Au/parylene (thickness: 5 μm/20 nm/300 nm/20 nm/50 nm/5 μm), followed by transfer onto a silicone elastomer (Ecoflex 00-30) by a water-soluble tape (Aquasol Corporation; NY, USA). The surgical procedures are the same as those for dorsal subcutaneous devices. After anchoring the interconnect with an adhesive conduit, stretching tests were performed with a pair of forceps to grasp the uncovered end. The mice were posed gently to bend the interconnect as a test of bending stability.

Ex vivo characterization of devices designed to interface with moving tissue surfaces

Evaluations of adhesion to wet, dynamic tissues used bioresorbable, wireless, battery-free, miniature pacemakers. The fabrication process followed steps described previously[22]. *Ex vivo* characterization involved an isolated chicken heart fixed on a modified vibration stage moving at 20 Hz with an amplitude to mimic the cyclic movement of a beating heart. Anchoring the pacing electrodes onto the surface of the heart with the BTIM during these motions demonstrated the ability to bond to a wet and dynamic curvilinear tissue surface. Soaking the entire system in PBS (pH 7.4) at 25 °C for two weeks validated the stability of this bond.

Surgical procedures for wireless systems designed for cardiac pacing

Fully implantable, bioresorbable, wireless, battery-free pacemakers were implanted into male and female adult rats (Sprague-Dawley and Long Evans). All surgeries were performed under general anesthesia with isoflurane. The rat's ECG was recorded by a PowerLab acquisition system and LabChart software (AD Instruments, Dunedin, New Zealand) in the standard Lead I configuration (left arm as the negative electrode, right arm as positive, and right leg as ground) to monitor the heart rate throughout the procedure. Animals were intubated with a 16-gauge blunt tip catheter and ventilated using the VentElite Small Animal Ventilator (Harvard Apparatus, MA, USA). The heart was exposed via the left thoracotomy. For animals in which the BTIM was used, the electrodes of the pacemaker were specially outfitted with a rectangular PLGA frame to allow for full contact between the electrodes and the tissue when placed onto the anterior epicardial surface. The primers and precursors were spread into the PLGA frame and polymerized by UV exposure for 3 min. For control animals that had the devices implanted using sutures, the electrode pad of the pacemaker was sutured onto the anterior epicardium using two interrupted monofilament sutures (Ethicon Inc., NJ, USA). The receiver of the pacemaker was placed into a subcutaneous pocket on the ventral aspect of the animal. The thoracic cavity, muscle, and skin were then closed in the ensuing layers using 6-0 nylon monofilament sutures (Ethicon Inc., NJ, USA). Pacing and capture of the heart to verify pacemaker functionality were confirmed by ECG signals immediately after device attachment and following closure. Animals were allowed to recover until recumbency was regained. Analgesic was provided every 12 h in the 48 h following surgery, along with appropriate postoperative care.

Evaluation of adhesive bonds and device functionality for cardiac pacing devices

Power was delivered to the pacemaker via wireless inductive power transfer. During each pacing session, a three-lead ECG in the Lead I configuration was recorded using LabChart software (AD Instruments, Dunedin, New Zealand). Heart rate was calculated from cyclic measurements of the R wave from the ECG. The resting heart rate in these cohorts was approximately 350 bpm. During implantation, animals were paced immediately following the deployment of the BTIM onto the heart and after the closure of muscle and skin. Post-operatively, animals were subjected to ventricular pacing at 600 bpm or higher, and an ECG was recorded to assess the device functionality. The pacing was performed until the pacemaker failed to drive the heart rhythm. Explanting the hearts that had pacemakers implanted with the BTIM at 10 days after surgery enabled observations and assessments of the level of adhesion. Stable and firm adhesion after 10 days post-surgery was verified by device explantation. A qualitative test of suspending and mechanically agitating the heart was employed to affirm the level of delamination between electrodes and the heart.

Evaluations of biocompatibility for BTIM-encapsulated cardiac pacing devices

Histological analysis—Growth of fibrotic tissue was evaluated for rats without implanted devices, with pacemakers implanted using sutures, and with pacemakers implanted using the BTIM. 4 weeks after implantation, hearts were excised and perfusion-fixed with 10% neutral buffered formalin. Tissue samples were then paraffin-embedded, sectioned, and stained with Masson’s trichrome. Images were collected at 4x using an EVOS XL light microscope (Thermo Fisher Scientific, MA, USA). The volume fractions of myocytes, collagen, and interstitial space were assessed for the transmural volume near the site of device attachment through MATLAB (MathWorks, MA, USA). Personnel performing analysis were blinded to group allocations. The amount of disorganized connective tissue on top of the myocardium, as observed during explantation, was evaluated by a double-blinded clinical-scoring system on a scale of 0 to 5. The scoring system was scaled as follows: no signs of scarring (0), minimal amounts of transparent scarring that is easily disrupted (1), small amounts of scar tissue that requires blunt instruments to disrupt (2), moderate amounts of opaque scarring that requires blunt instruments to disrupt (3), dense scar tissue that requires sharp instrumentation to disrupt (4), and very dense scar tissue that grossly distorts heart anatomy (5). A Kruskal-Wallis statistical test was used to compare volume fractions and clinical scores outcomes, respectively, between the control, suture, and BTIM groups where $p < 0.05$ was considered as statistically significant.

MicroCT and MRI analysis—All procedures, including data visualization and image registration, were similar to those previously described for deep brain optogenetics.

Fabrication process for systems designed for cardiac electrophysiology mapping

A thin, flexible electrode array with 64 channels served as the platform for cardiac electrophysiology mapping. The fabrication process began with coating a layer of parylene (thickness: 4 μm) on a glass slide. A lift-off process defined patterns for the electrodes and interconnects in Cr/Au (thickness: 10/100 nm). Deposition of another layer of parylene (thickness: 4 μm) covered the metal pattern. Photolithography (AZ4620; thickness: ~ 10

μm) and oxygen plasma etching (March RIE) removed regions of the parylene to expose the metal electrodes. Carefully peeling the electrode array from the glass substrate after thermally anchoring a 15-cm-long anisotropic conductive film on the connection pads completed the process.

Surgical procedures for systems designed for cardiac electrophysiology mapping

All animal procedures were performed according to protocols approved by the Institutional Animal Care and Use Committee Rabbits of The George Washington University. Rabbits were first anesthetized with a mixture of ketamine and xylazine, and isoflurane vapors were administered to deepen the anesthesia further. A dose of heparin was administered intravenously by ear vein injection. Cessation of pain was confirmed via toe pinch, and then the heart was excised via sternal thoracotomy. The heart was immediately cannulated in UW cardioplegia solution via the aorta and placed into a constant-pressure Langendorff system perfused with a modified Tyrode's solution (in mM: 128.2 NaCl, 4.7 KCl, 1.05 $MgCl_2$, 1.3 $CaCl_2$, 1.19 NaH_2PO_4, 20 $NaHCO_3$, and 11.1 glucose) at 37°C that was bubbled with 95% O_2/ 5% CO_2. The heart was allowed to recover for 5-10 minutes. Following the recovery period, the excitation-contraction uncoupler, blebbistatin (Cayman Chemical, MI, USA), was administered so that the working concentration in the system was at 10 μM. A voltage-sensitive dye (125 nM), di-4-ANEPPS (excitation/emission spectra 520/650), was added at an upstream bubble trap to stain the tissue. As a control, the ultrathin, flexible 64-electrode array was applied with no adhesive encapsulation or adhesive interface to the heart.

For the encapsulation method, the electrode array was first placed on the epicardium, and then the primer and precursor mixtures were applied to coat the device to the adjacent tissue. Exposure to UV light cured the BTIM. For the interface method, forming amine functional groups on the parylene surfaces of the device followed the procedures mentioned above. Applying primer and precursor mixture onto the epicardium, placing the array on top, and then exposing to UV completed the process.

Evaluation of functionality of devices for cardiac electrophysiology mapping

After applying the BTIM by the encapsulation or interface methods, connections between the array and an Intan 1024-channel recording controller occurred through two 36-pin wire adapters, a 64-channel amplifier board (RHD2164), and a serial peripheral interface (SPI) cable via a 15-cm-long anisotropic conductive film (ACF), laser-defined printed circuit board (PCB), a zero insertion force (ZIF) interconnector and another customized PCB. A commercial software interface simultaneously recorded electrograms across all 64 channels at a sampling rate of 20 kS/s, across a frequency range of 0.1 to 200 Hz with a notch filter at 60 Hz. A high-speed CMOS camera with the MiCAM05 system (SciMedia, CA, USA) optically mapped the cardiac tissue membrane potential (sampling frequency: 1 kHz) by exciting the voltage-sensitive dye-stained tissue using a 520 nm green light (Prizmatix, Israel). Passing a digital pulse from the MiCAM05 to the Intan system triggered synchronized recording of the electrical signals and optical signals with the respective systems.

Statistical analysis

Statistical significance and *P* values of Fig. 3k, Extended Data Fig. 6b-c, Supplementary Fig. 17, and Supplementary Fig. 18 are determined by two-sided Student's *t*-test using Microsoft Excel. Statistical significance and *P* values of Fig. 5f-g are determined Kruskal-Wallis test and Post-hoc Dunn's multiple comparison test using Statsoft. Statistical significance and *P* values of Fig. 6f-g are determined by Wilcoxon matched pairs signed-rank test using Statsoft. Statistical significance and *P* values of Extended Data Fig. 2f are determined by one-way ANOVA using GraphPad Prism. The significance thresholds were $*P \leq 0.05$. ns indicates no statistically significant differences.

Reporting summary

Further information on research design is available in the Nature Research Reporting Summary linked to this article.

Data availability

Source data are provided with this paper. All other data that support the results in this study are available from the corresponding author upon reasonable request.

Code availability

Software for the analysis of optical mapping data, RHYHTM, is openly available for free download at https://github.com/optocardiography. Other custom codes used in this study are available from the corresponding author upon reasonable request.

Extended Data

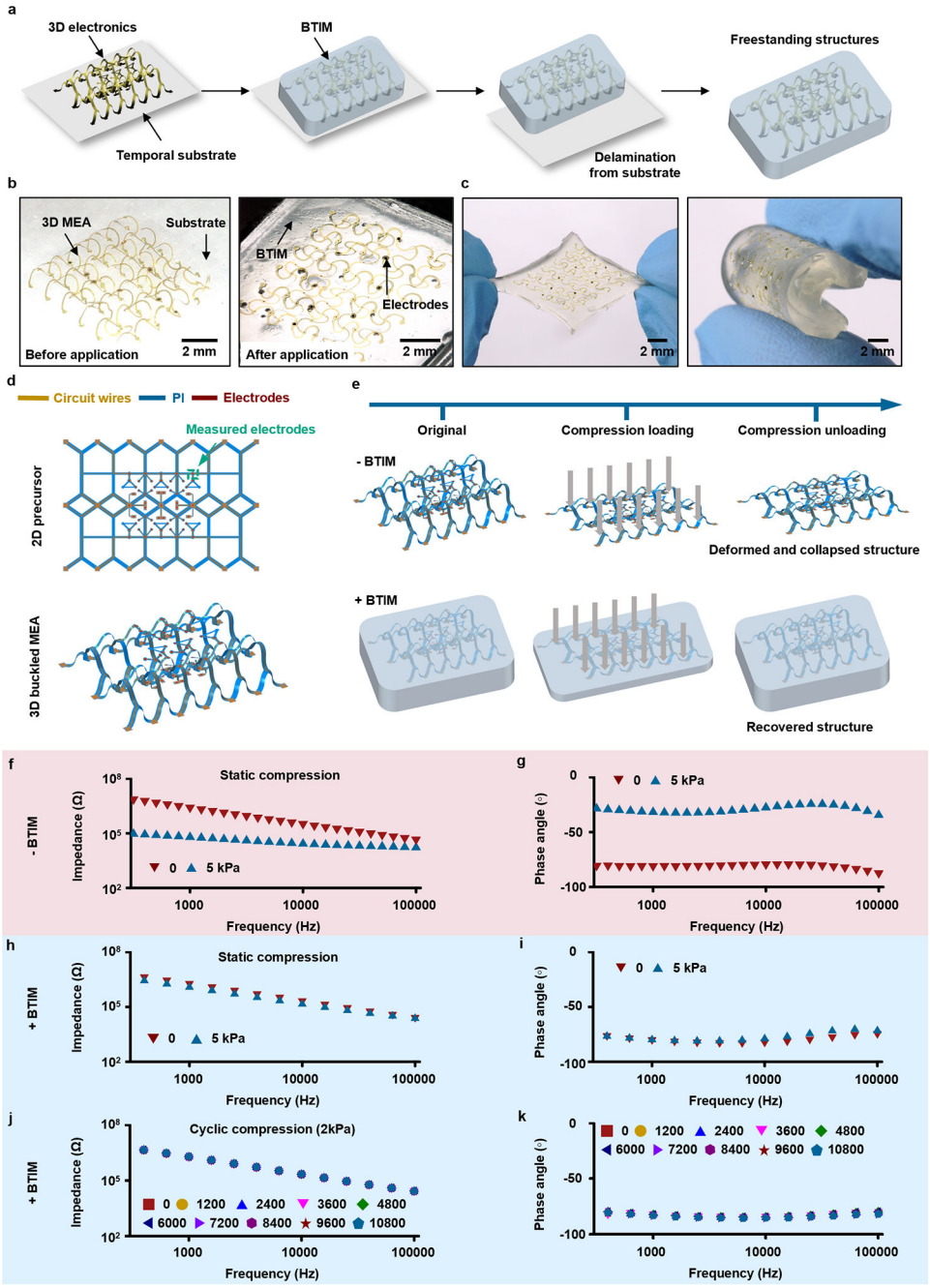

Extended Data Fig. 1 |. Supporting matrices for electrode-embedded 3D electronic systems. **a,** Schematic illustration of procedures to integrate 3D electronics into a matrix of the BTIM. The matrix allows manual manipulation without damaging fragile features, with the ability to bond to dynamic, curved tissue surfaces. **b,** Image of a 3D device formed by compressive buckling on an elastomer substrate. **c,** Micrograph of a 3D device in a BTIM supporting matrix. **d,** Schematic illustrations of the 2D precursor before compressive buckling (first panel) and the 3D structure after compressive buckling (second panel), with the measuring

electrode in the central area. **e,** Schematic illustration of the original and deformed status of the non-encapsulated (first row) and the BTIM-encapsulated (second row) 3D MEAs under compressive pressure. **f, g,** Curves for impedance and phase angle over the frequency sweep without the BTIM before and after compressive pressure. **h, i,** Impedance and phase angle over the frequency sweep with the BTIM under static compression fatigue tests. **j, k,** Impedance and phase angle over the frequency sweep with the BTIM under dynamic compression fatigue tests (pressure: 2 kPa; cycle number: 10^4).

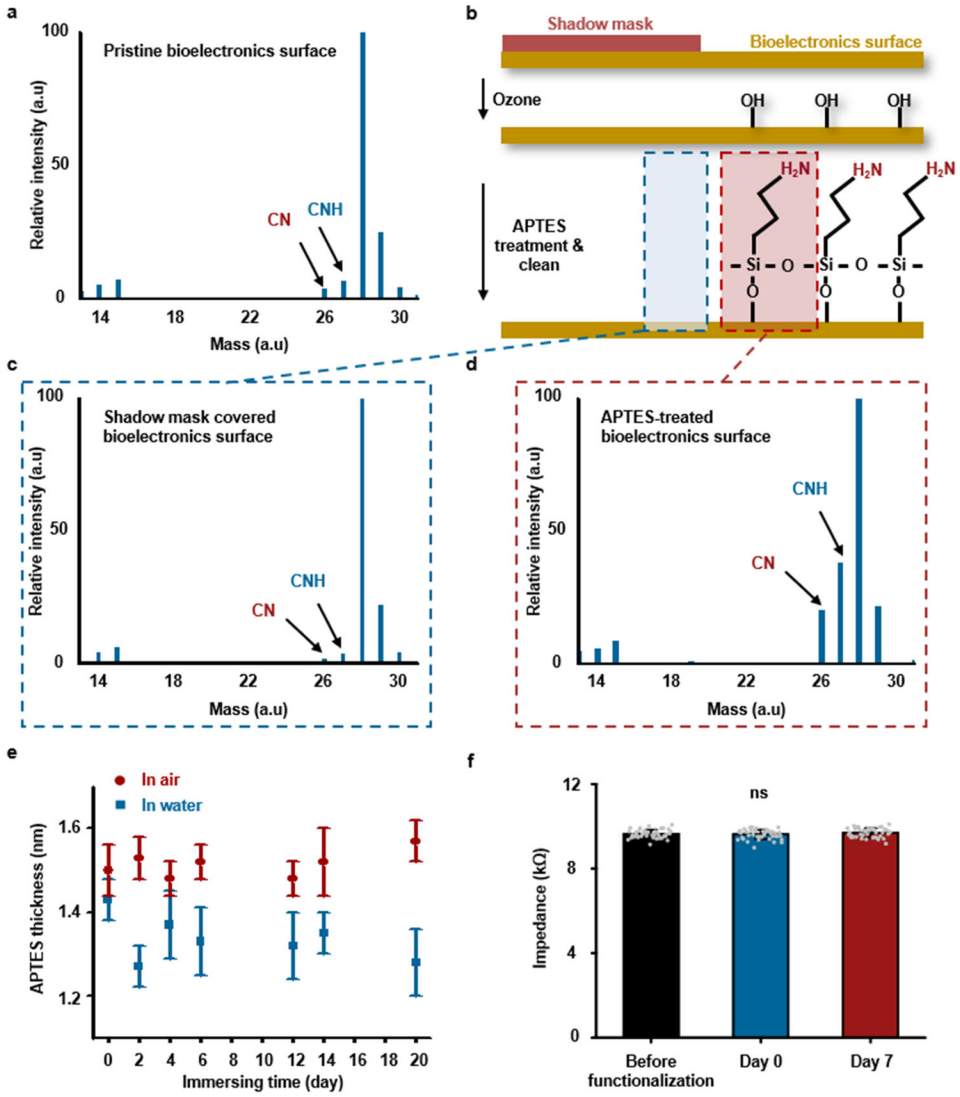

Extended Data Fig. 2 |. Influence of APTES-functionalization on bioelectronics surfaces. **a,** ToF-SIMS analysis of a representative pristine bioelectronic surface (PLA). **b,** Steps for selective functionalization of this surface through a patterned polyimide adhesive-coated shadow mask. **c,** ToF-SIMS analysis on the shadowed area of the surface shows results that are similar to those from the pristine surface. **d,** ToF-SIMS analysis of the exposed area of the bioelectronic surface. To normalize the intensity, the intensity I_{28}, where the mass is 28, was set as 100 and calculate the relative intensity of each case. **e,** Thickness of an

APTES layer formed on a silicon wafer exposed in air and submerged in water as a function of time after formation. Spectroscopic ellipsometry was used for these measurements. **f, Impedance of MEA electrodes at 1 kHz in 0.1 M PBS at room temperature before APTES** functionalization **and immediately and 7 days after APTES** functionalization ($F(2,123) = 0.0201$, $P = 0.9801$). $n = 6$ independent samples in **e** and $n = 40$ independent electrodes from 10 independent devices and 3 independent batches in **f**. Values in **e** and **f** represent the mean ± standard deviation. Statistical significance and P values are determined by one-way ANOVA at a significance level of 0.05. ns indicates no statistically significant differences.

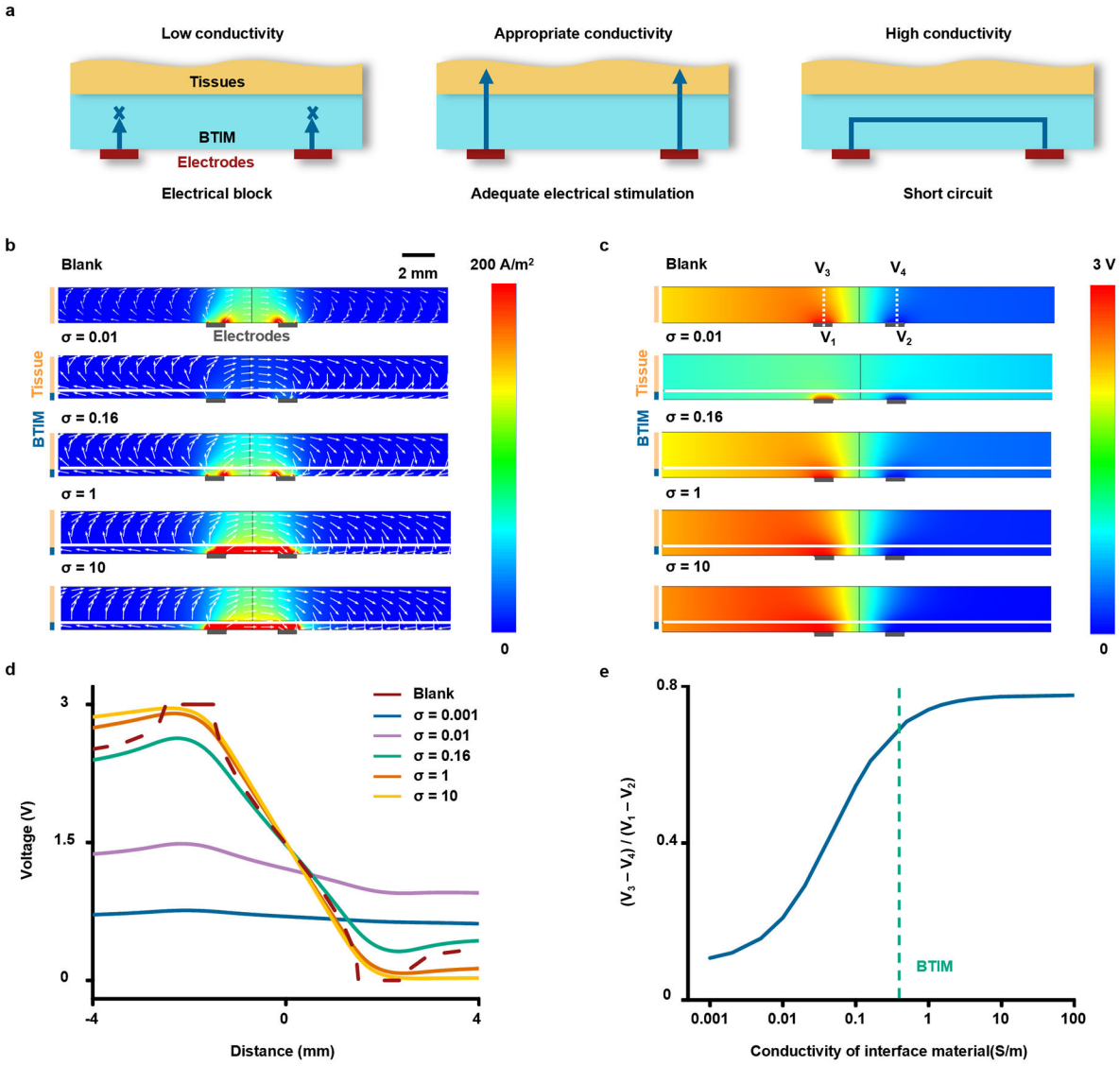

Extended Data Fig. 3 |. Analysis of electrical distribution on electrical stimulation.
a, Influence of the conductivity of the interface material on electrical stimulation. **b,** Current density distributions in the myocardium layer and the interface material with different conductivities. **c,** Potential distribution in the myocardium layer and the interface material

with different conductivities. **d,** Corresponding potential distributions on the top of the myocardium layer as a function of the interface material conductivity. **e,** Ratio of the potential difference on the tissues ($V_3 - V_4$) to the corresponding potential difference on the electrodes ($V_1 - V_2$, 3V) as a function of the interface material conductivity.

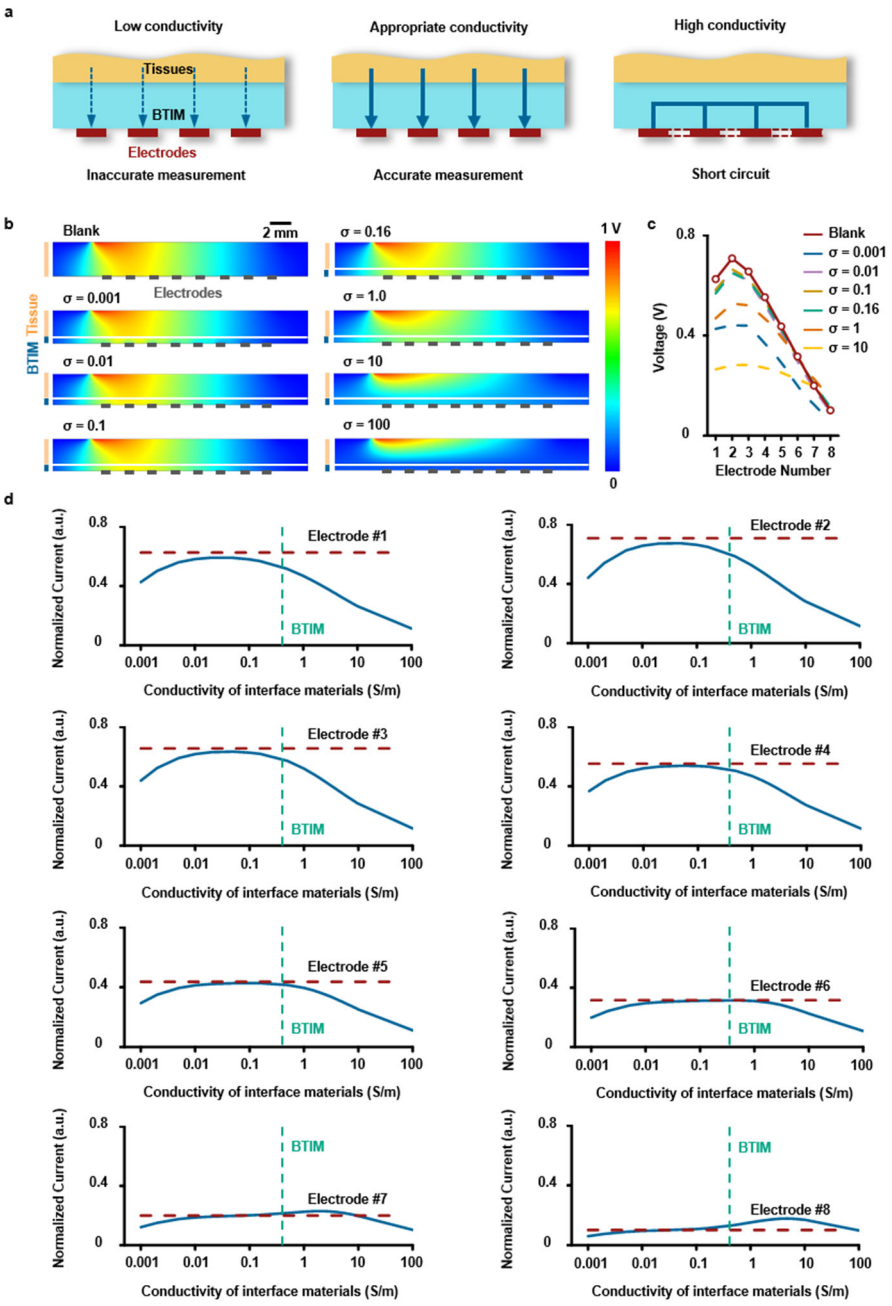

Extended Data Fig. 4 |. Analysis of electrical distribution on biopotential mapping.
a, Influence of the conductivity of the BTIM on biopotential mapping. **b,** Biopotential distribution in the myocardium layer and the interface material layer with various conductivities. **c,** Calculated potential at all of the electrodes for different conductivities.

d, Calculated potential on all the electrodes in the presence of the interface material layer with various conductivities (blue solid line) and in the absence of the interface material layer (red dash line).

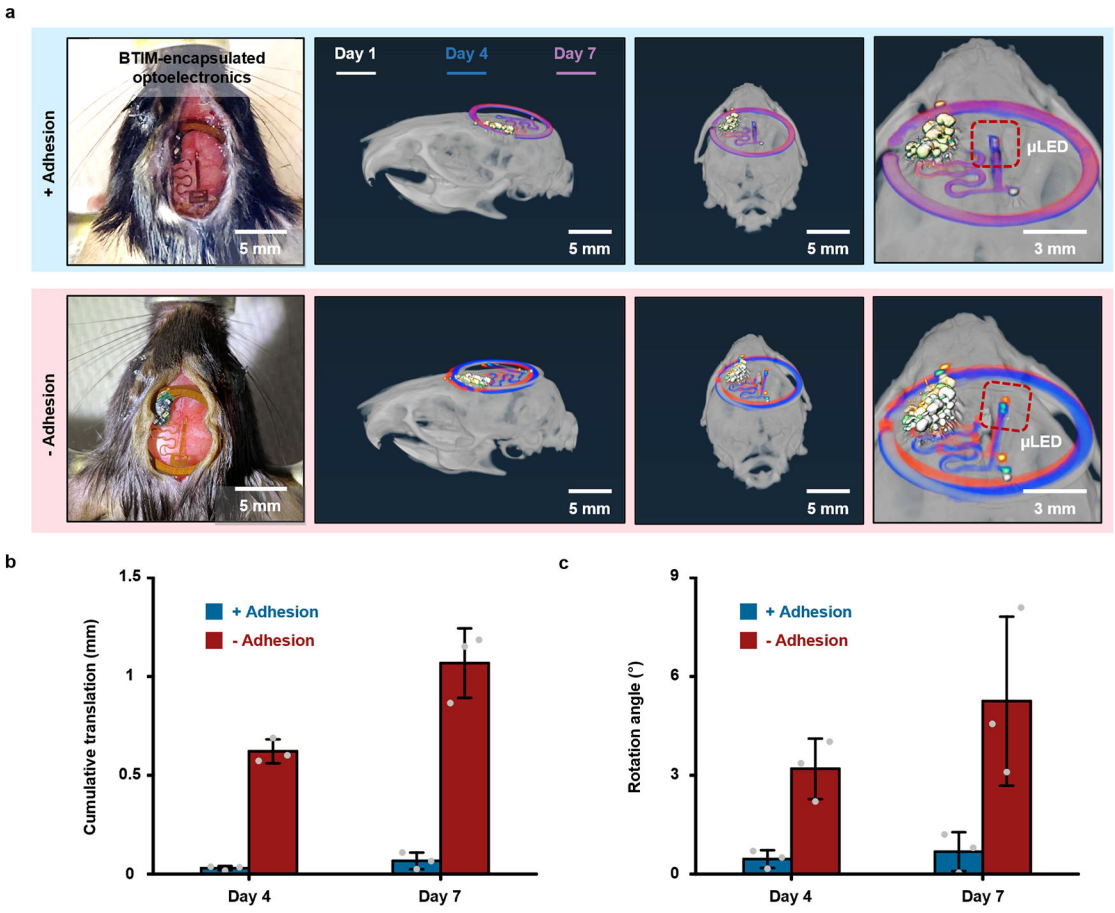

Extended Data Fig. 5 | Mechanical stability of the BTIM-encapsulated wireless optoelectronics. **a,** Original device position determined by the photographs, and positions of BTIM-encapsulated devices (first row) and non-adhesive (second row) devices on day 1 (white), 4 (blue), and 7 (purple) post-surgery determined by MicroCT. **b, c,** Statistical analyses of the net translations (**b**) and rotations (**c**) of the μ-ILED in the BTIM-encapsulated (blue) and non-adhesive devices (red) on day 4 and 7 compared with those on day 1 post-surgery. $n = 3$ biologically independent animals. Values in **b**-**c** represent the mean ± standard deviation.

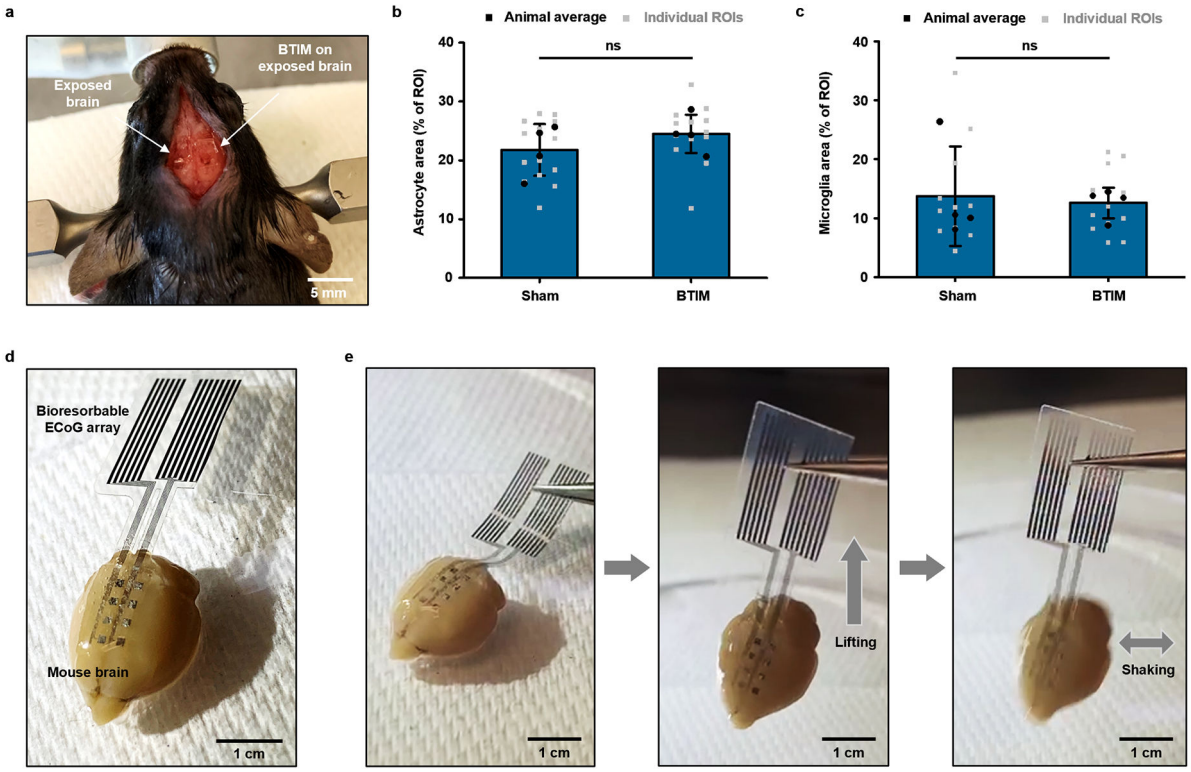

Extended Data Fig. 6 |. Applying BTIM on brain-related bioelectronics/optoelectronics.
a, Image of the brain areas exposed to the BTIM. **b, c,** Astrocyte area percentages and microglia area percentages for the sham group and the BTIM group. Black dots: animal average. Black dots: animal average, 4 animals in total. Grey dots: individual ROIs. 10 – 12 ROIs from 4 animals in total, 2 – 3 ROIs from each animal. $P = 0.3546$ in **b** and $P = 0.8049$ in **c**. **d,** The image of the BTIM-encapsulated b-MEA on a mouse brain *ex vivo*. **e,** Robust adhesion even when the b-MEA is lifted or shaken. $n = 12$ independent measurements from 4 biologically independent animals in **b-c**. Values in **b-c** represent the mean ± standard deviation. Statistical significance and P values are determined by two-sided Student's t-test at a significance level of 0.05. ns indicates no statistically significant differences.

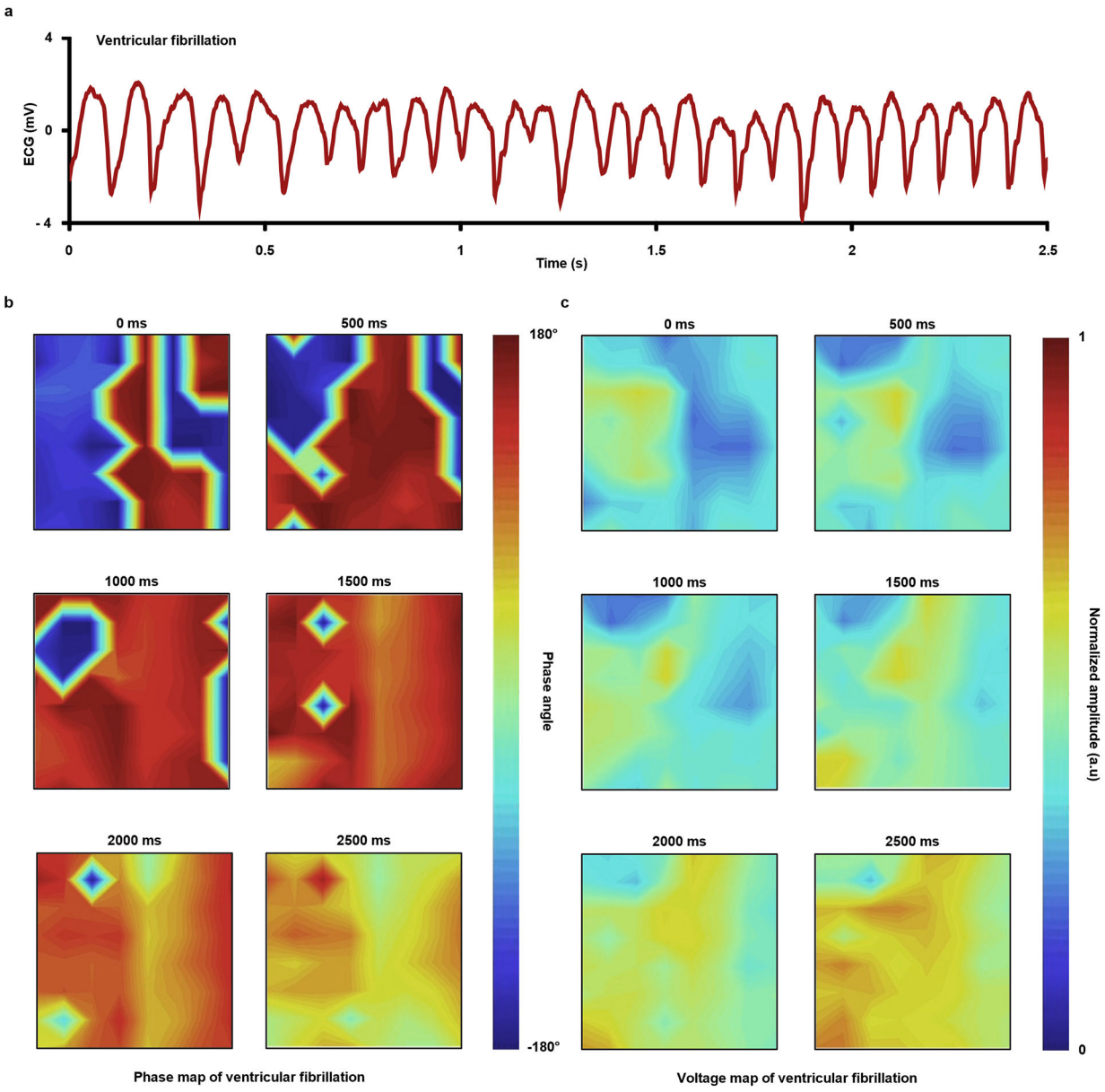

Extended Data Fig. 7 |. Electrogram signals of ventricular fibrillation from an MEA with BTIM encapsulation.

a, Representative electrogram signal collected from a Langendorff-perfused rabbit heart during ventricular fibrillation (VF). **b, c,** Phase (**b**) and voltage (**c**) map of VF over 2500 ms.

Supplementary Material

Refer to Web version on PubMed Central for supplementary material.

Acknowledgments

This work was generously funded by the Leducq Foundation project RHYTHM and the National Institutes of Health (R01-HL141470 to I.R.E. and J.A.R.). This work made use of the NUFAB facility of Northwestern University's NUANCE Center, which has received support from the Soft and Hybrid Nanotechnology Experimental

(SHyNE) Resource (NSF ECCS-2025633); the MRSEC program (NSF DMR-1720139) at the Materials Research Center; the International Institute for Nanotechnology (IIN); the Keck Foundation; the Querrey Simpson Institute for Bioelectronics; the Keck Biophysics Facility, a shared resource of the Robert H. Lurie Comprehensive Cancer Center of Northwestern University, which has received support in part by the NCI Cancer Center Support (P30 CA060553); the Center for Advanced Molecular Imaging (RRID:SCR_021192); Northwestern University; and the State of Illinois, through the IIN. R.T.Y. acknowledges support from the American Heart Association (19PRE34380781). M.W acknowledges support from the National Institutes of Health (T32 AG20506). Z.X. acknowledges the support from the National Natural Science Foundation of China (12072057), LiaoNing Revitalization Talents Program (XLYC2007196) and Fundamental Research Funds for the Central Universities (DUT20RC(3)032). K.A. acknowledges support from the National Institutes of Health (5K99-HL148523-02). Y.H. acknowledges support from the National Foundation of Science (CMMI1635443). Y.K. acknowledges support from National Institutes of Health (R01NS107539 and R01MH117111), Beckman Young Investigator Award, Rita Allen Foundation Scholar Award, and Searle Scholar Award. The diagrams of mouse body with organs in Fig. 1f are created with © BioRender – biorender.com.

References

1. Kalantar-Zadeh K et al. A human pilot trial of ingestible electronic capsules capable of sensing different gases in the gut. Nature Electronics 1, 79–87 (2018).
2. Dagdeviren C et al. Flexible piezoelectric devices for gastrointestinal motility sensing. Nature Biomedical Engineering 1, 807–817 (2017).
3. Feiner R et al. Engineered hybrid cardiac patches with multifunctional electronics for online monitoring and regulation of tissue function. Nature Materials 15, 679–685 (2016). [PubMed: 26974408]
4. Jun JJ et al. Fully integrated silicon probes for high-density recording of neural activity. Nature 551, 232–236 (2017). [PubMed: 29120427]
5. Mickle AD et al. A wireless closed-loop system for optogenetic peripheral neuromodulation. Nature 565, 361–365 (2019). [PubMed: 30602791]
6. Feiner R & Dvir T Tissue–electronics interfaces: from implantable devices to engineered tissues. Nature Reviews Materials 3, 17076 (2018).
7. Yang C & Suo Z Hydrogel ionotronics. Nature Reviews Materials 3, 125–142 (2018).
8. Yuk H, Lu B & Zhao X Hydrogel bioelectronics. Chemical Society Reviews 48, 1642–1667 (2019). [PubMed: 30474663]
9. Global wound closure products market expecteprimaru d to be worth US $ 15 billion by 2022. Market Research Engine (2018).
10. Potvin R, Matossian C & Makari S Cataract surgery and methods of wound closure: a review. Clinical Ophthalmology 921 (2015) doi:10.2147/OPTH.S83552. [PubMed: 26045656]
11. Edmiston CE et al. Microbiology of explanted suture segments from infected and noninfected surgical patients. Journal of Clinical Microbiology 51, 417–421 (2013). [PubMed: 23175247]
12. Owens CD & Stoessel K Surgical site infections: epidemiology, microbiology and prevention. Journal of Hospital Infection 70, 3–10 (2008).
13. Mond HG, Helland JR, Stokes K, Bornzin GA & McVenes R The electrode-tissue interface: the revolutionary role of steroid-elution. Pacing and Clinical Electrophysiology 37, 1232–1249 (2014). [PubMed: 25130977]
14. Yuk H et al. Dry double-sided tape for adhesion of wet tissues and devices. Nature 575, 169–174 (2019). [PubMed: 31666696]
15. Li J et al. Tough adhesives for diverse wet surfaces. Science 357, 378–381 (2017). [PubMed: 28751604]
16. Lin X et al. A viscoelastic adhesive epicardial patch for treating myocardial infarction. Nature Biomedical Engineering 3, 632–643 (2019).
17. Liang S et al. Paintable and rapidly bondable conductive hydrogels as therapeutic cardiac patches. Advanced Materials 30, 1704235 (2018).
18. Gan D et al. Plant-inspired adhesive and tough hydrogel based on Ag-Lignin nanoparticles-triggered dynamic redox catechol chemistry. Nature Communications 10, 1487 (2019).
19. Blacklow SO et al. Bioinspired mechanically active adhesive dressings to accelerate wound closure. Science Advances 5, eaaw3963 (2019). [PubMed: 31355332]

20. Wang X et al. Three-dimensional electronic scaffolds for monitoring and regulation of multifunctional hybrid tissues. Extreme Mechanics Letters 35, 100634 (2020).
21. Shin G et al. Flexible near-field wireless optoelectronics as subdermal implants for broad applications in optogenetics. Neuron 93, 509–521.e3 (2017). [PubMed: 28132830]
22. Koo J et al. Wireless bioresorbable electronic system enables sustained nonpharmacological neuroregenerative therapy. Nature Medicine 24, 1830–1836 (2018).
23. Yu KJ et al. Bioresorbable silicon electronics for transient spatiotemporal mapping of electrical activity from the cerebral cortex. Nature Materials 15, 782–791 (2016). [PubMed: 27088236]
24. Mathur AB, Collinsworth AM, Reichert WM, Kraus WE & Truskey GA Endothelial, cardiac muscle and skeletal muscle exhibit different viscous and elastic properties as determined by atomic force microscopy. Journal of Biomechanics 34, 1545–1553 (2001). [PubMed: 11716856]
25. Arda K, Ciledag N, Aktas E, Arıbas BK & Köse K Quantitative assessment of normal soft-tissue elasticity using shear-wave ultrasound elastography. American Journal of Roentgenology 197, 532–536 (2011). [PubMed: 21862792]
26. Yanniotis S, Skaltsi S & Karaburnioti S Effect of moisture content on the viscosity of honey at different temperatures. Journal of Food Engineering 72, 372–377 (2006).
27. Kang S-K et al. Bioresorbable silicon electronic sensors for the brain. Nature 530, 71–76 (2016). [PubMed: 26779949]
28. Yamagishi K et al. Tissue-adhesive wirelessly powered optoelectronic device for metronomic photodynamic cancer therapy. Nature Biomedical Engineering 3, 27–36 (2019).
29. Zhang Y et al. Battery-free, lightweight, injectable microsystem for in vivo wireless pharmacology and optogenetics. Proceedings of the National Academy of Sciences 116, 21427–21437 (2019).
30. Gutruf P et al. Fully implantable optoelectronic systems for battery-free, multimodal operation in neuroscience research. Nature Electronics 1, 652–660 (2018).
31. Burton A et al. Wireless, battery-free subdermally implantable photometry systems for chronic recording of neural dynamics. Proceedings of the National Academy of Sciences 117, 2835–2845 (2020).
32. Bai W et al. Bioresorbable photonic devices for the spectroscopic characterization of physiological status and neural activity. Nature Biomedical Engineering 3, 644–654 (2019).
33. Tharanathan RN Biodegradable films and composite coatings: past, present and future. Trends in Food Science & Technology 14, 71–78 (2003).
34. Boutry CM et al. Towards biodegradable wireless implants. Philosophical Transactions of the Royal Society A: Mathematical, Physical and Engineering Sciences 370, 2418–2432 (2012).
35. Chen T-W et al. Ultrasensitive fluorescent proteins for imaging neuronal activity. Nature 499, 295–300 (2013). [PubMed: 23868258]
36. Yang Y et al. Wireless multilateral devices for optogenetic studies of individual and social behaviors. Nature Neuroscience (2021) doi:10.1038/s41593-021-00849-x.
37. Fang H et al. Capacitively coupled arrays of multiplexed flexible silicon transistors for long-term cardiac electrophysiology. Nature Biomedical Engineering 1, 0038 (2017).
38. Lee W et al. Nonthrombogenic, stretchable, active multielectrode array for electroanatomical mapping. Science Advances 4, eaau2426 (2018). [PubMed: 30345362]
39. Sawhney AS, Pathak CP & Hubbell JA Bioerodible hydrogels based on photopolymerized poly(ethylene glycol)-co-poly(.alpha.-hydroxy acid) diacrylate macromers. Macromolecules 26, 581–587 (1993).
40. Sun J-Y et al. Highly stretchable and tough hydrogels. Nature 489, 133–136 (2012). [PubMed: 22955625]
41. Gong JP et al. Synthesis of hydrogels with extremely low surface friction. Journal of the American Chemical Society 123, 5582–5583 (2001). [PubMed: 11389644]
42. Rudy A et al. Lubricous hydrogel surface coatings on polydimethylsiloxane (PDMS). Tribology Letters 65, 3 (2017).
43. Schneider CA, Rasband WS & Eliceiri KW NIH Image to ImageJ: 25 years of image analysis. Nature Methods 9, 671–675 (2012). [PubMed: 22930834]

44. Rodriguez A et al. ToxTrac : A fast and robust software for tracking organisms. Methods in Ecology and Evolution 9, 460–464 (2018).

45. Schindelin J et al. Fiji: an open-source platform for biological-image analysis. Nature Methods 9, 676–682 (2012). [PubMed: 22743772]

46. Wu M et al. Attenuated dopamine signaling after aversive learning is restored by ketamine to rescue escape actions. eLife 10, (2021).

47. Wu M, Minkowicz S, Dumrongprechachan V, Hamilton P & Kozorovitskiy Y Ketamine rapidly enhances glutamate-evoked dendritic spinogenesis in medial prefrontal cortex through dopaminergic mechanisms. Biological Psychiatry 89, 1096–1105 (2021). [PubMed: 33637303]

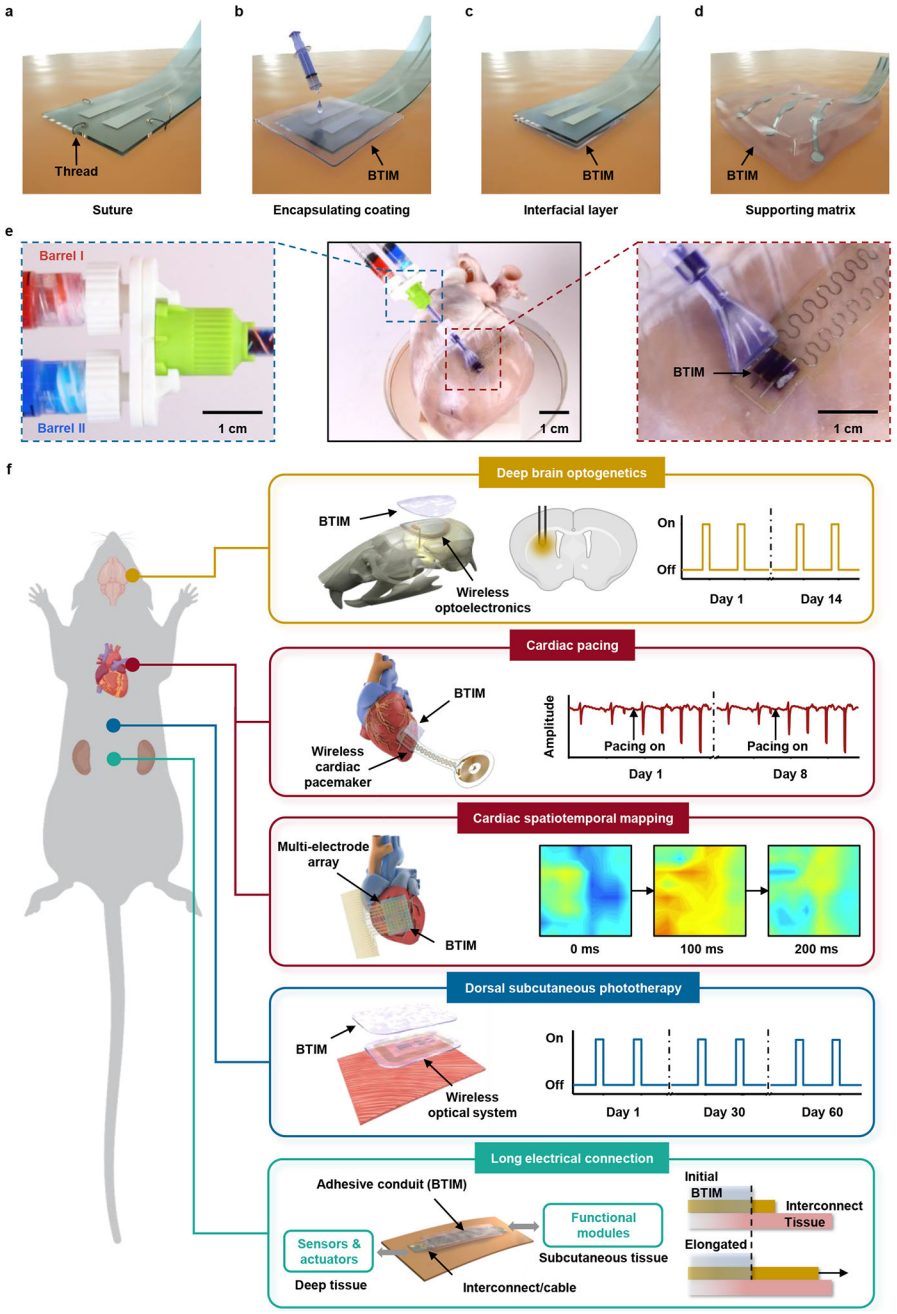

Fig. 1 |. Soft interface materials for joining bioelectronics devices with biological tissues. **a-d,** Schematic illustrations of a conventional suturing process (**a**) and three alternative schemes based on the BTIM, including encapsulating coatings (**b**), interfacial layers (**c**), and supporting matrices (**d**). **e,** Procedures for applying this two-component adhesive chemistry onto a porcine heart to anchor a pair of electrodes via the encapsulation scheme. Blue inset: precursors in barrel I (dyed in red; PEG-LA-DA, Ca^{2+}, and photo-initiators) and barrel II (dyed in blue; SA) of a dual-syringe delivery system mix as they pass through the shaft and emerge at the tip end, highlighted in purple. Red inset: Applying the resulting liquid mixture onto tissue coated with primer, followed by curing into a solid form by exposure to UV light

(wavelength: 365 nm; density: 20 mW/cm^2; duration: 3 min) to complete the encapsulation process. **f,** Seamless integration of electronic and optoelectronic systems onto the surfaces of living tissues, with robust adhesion for stable electrical and/or optical interfaces across dermal, neuronal, and cardiac applications for several days to months.

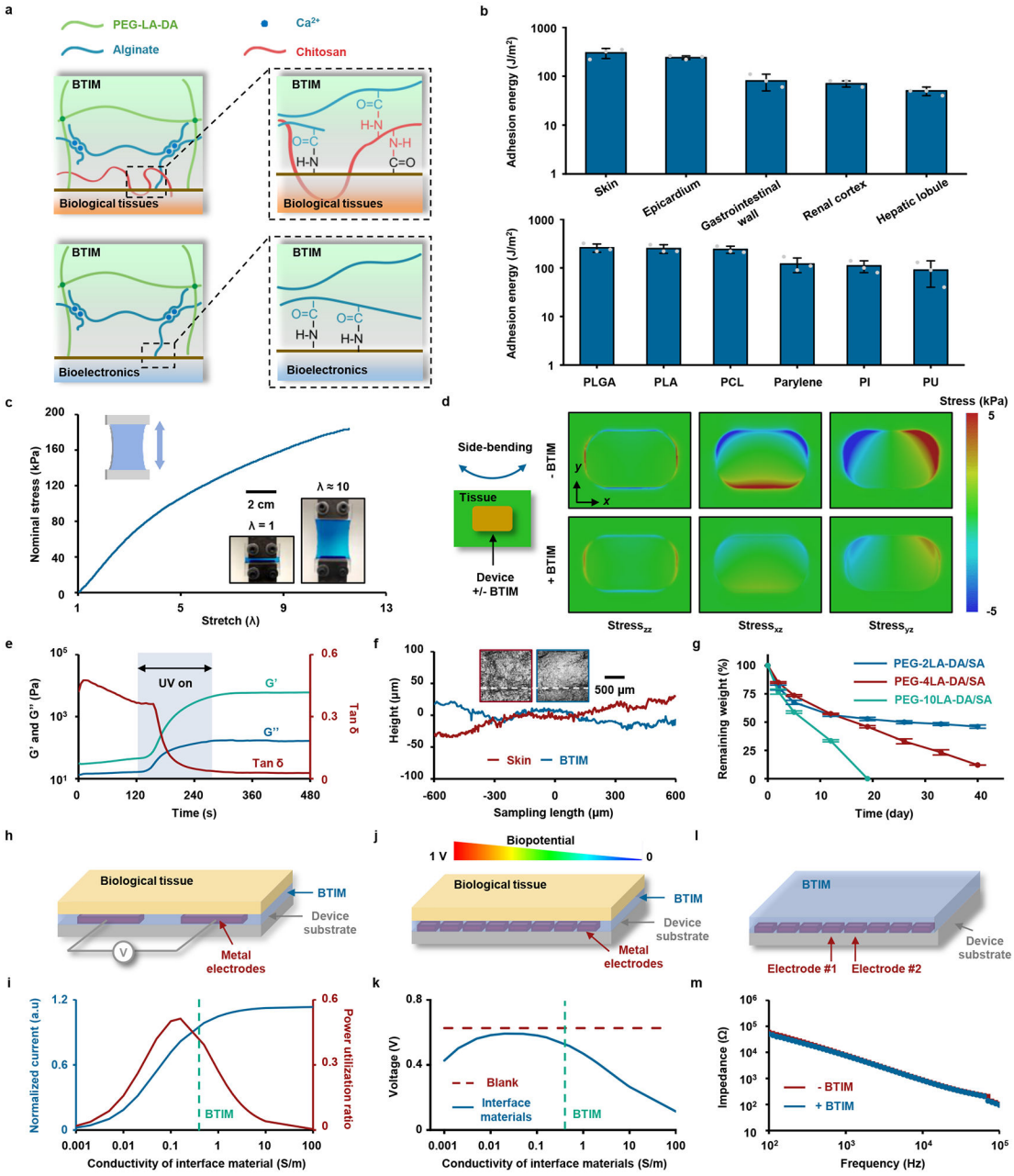

Fig. 2 |. Key characteristics of the BTIM.

Adhesion properties. a, Mechanisms of interfacial bonding to the surfaces of biological tissues (first panel) and bioelectronics devices (second panel). **b,** Adhesion energy between BTIM and a variety of tissues or device surfaces. **Mechanical properties. c,** Stress-strain curves from samples of the BTIM. Inset: images of a BTIM specimen (colored in blue) before and after elongation without fracture. **d,** Distribution of shear and normal stresses at the interface between a representative bioelectronic device (modulus: 2 GPa) and underlying tissues (modulus: 50 kPa) associated with side-bending (45°), determined by finite element analysis. The layer of the BTIM (thickness: 500 μm) decreases the maximum stresses by factors of 3.5, 3.3, and 3.3 for the zz, xz and yz components of the stress, respectively.

Photoinitiated gelation. e. Photoinitiated transformation of viscous liquid precursors to elastic crosslinked solid adhesives occurs upon UV exposure for 180 s. **f,** Conformal coating of the BTIM on a piece of porcine skin resulting from this photoinitiated liquid to solid transformation. Surface height profiles of the porcine skin and the BTIM are along the white line in each corresponding 3D confocal optical image in the inset. **Bioresorbability. g,** Remaining weights of BTIM with PEG-2LA-DA/SA (blue), PEG-4LA-DA/SA (red), and PEG-10LA-DA/SA (green) immersed in PBS (pH 7.4, 37 °C) as a function of time. **h,** Schematic illustration of the working conditions for BTIM-assisted electrical stimulation. **i,** Calculated normalized current and power utilization ratio on the top surface of the myocardium layer as a function of the interface material conductivity. The values are normalized by those in the absence of the interface material. **j,** Schematic illustration of the working conditions of BTIM-assisted biopotential mapping. **k,** Calculated potential on the electrode on the left side in the presence of the interface materials with various conductivities (blue) and in the absence of the materials (red). **l,** Schematic illustration of the experimental setup to measure the impedance between two adjacent MEA electrodes. **m,** Representative impedance spectra of two adjacent MEA electrodes before (blue) and after (red) BTIM application in 0.1 M PBS at room temperature. $n = 3$ independent samples in **b** and **g**. Values in **b** and **g** represent the mean ± standard deviation.

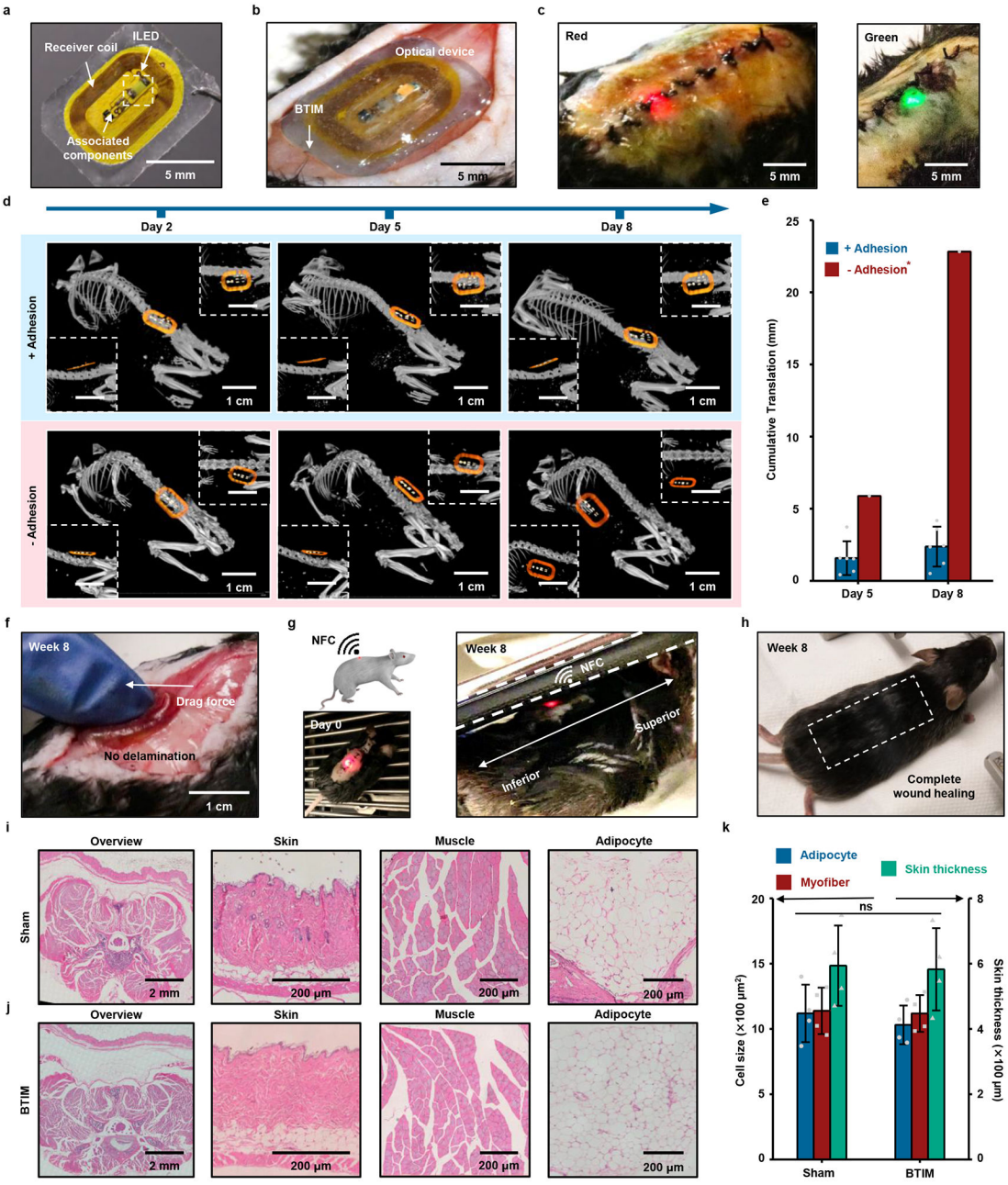

Fig. 3 | Soft adhesive interfaces between wireless optoelectronics and dorsal subcutaneous tissues.

a, Image of a device (10 mm × 6 mm × 1 mm) that includes an inductive loop antenna, an ILED, and associated electronic components. **b,** BTIM bonds the device to the dorsal subcutaneous area in a mouse model using the encapsulation strategy (adhesive size: 12 mm × 8 mm × 500 μm; colored in blue). **c,** Wireless activation of red (peak wavelength: 630 nm) and green (peak wavelength: 530 nm) ILEDs, which are selected for their relevance in tumor irradiation in dorsal subdermal tissues. **d,** Positions of encapsulated devices along the diagonal (main), sagittal (first inset), and coronal (second inset) directions at day 2, 5, and 8 post-surgery as determined by MicroCT. Hydrogels with the same chemical formulations

but without the use of a primer serve as the control group. **e,** Statistical analysis of the displacements of devices encapsulated using the BTIM with primer (blue) and without (red). *Two of the three devices in the second case exit the animal within 3 days post-surgery. **f,** Image illustrating robust adhesion after two months post-surgery in a manual stress test. **g,** Schematic illustration and image of wireless light activation in a chamber based on near-field communication (NFC) technology immediately after surgery (first panel) and after two months post-surgery (second panel). **h,** Image of complete wound healing of the surgical site after several weeks with fur regrown. **i, j**, H&E stains of the dorsal overview, skin, muscle, and adipocyte in sham (**i**) and BTIM (**j**) groups 1 month post-surgery. **k,** Statistical analyses of the adipocyte cell size, myofiber cell size, and the skin thickness in both groups. Both the cell sizes and the skin thickness present no significant differences between sham and BTIM groups ($P = 0.5324$ for adipocyte cell size, $P = 0.8650$ for myofiber cell size, and $P = 0.9035$ for skin thickness). $n = 6$ biologically independent animals for "+ Adhesion" group and $n=3$ biologically independent animals for "− Adhesion" group in **a-h**, and $n = 4$ biologically independent animals in **i-k**. Values in **e** and **k** represent the mean ± standard deviation. Statistical significance and P values are determined by two-sided Student's t-test at a significance level of 0.05. ns indicates no statistically significant differences.

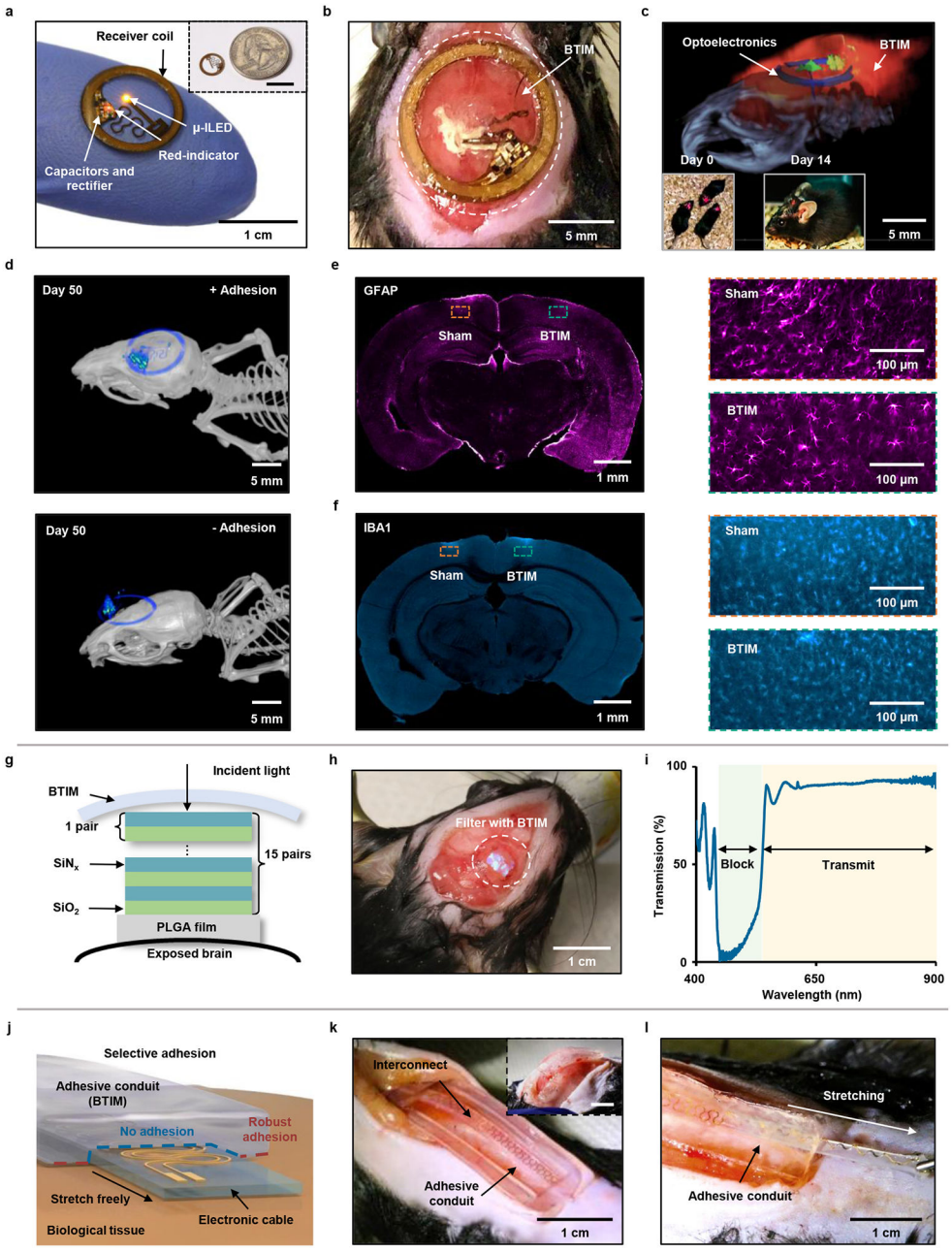

Fig. 4 |. Securing optical devices onto the brain and forming adhesives conduits for interconnects. **Wireless optogenetic devices. a,** Image of a thin, battery-free wireless device that includes a filamentary probe with a μ-ILED (wavelength: 590 nm) Inset: image of a device placed near a quarter. **b,** Stable positioning of the receiver coil and interconnects secured by the BTIM. **c,** Visualization of implanted devices through a combined image that overlays magnetic resonance imaging (MRI) slices with MicroCT reconstructions after two weeks post-surgery. Inset: Deep tissue optogenetic stimulation immediately after surgical implantation (first inset) and at 14 post-surgery days (second inset). **d,** MicroCT images of the BTIM-encapsulated (first panel) and non-adhesive (second panel) devices on the skull for transcranial optical stimulation day 50 post-surgery. **e, f,** GFAP (**e**; colored magenta)

and IBA1 (**f**; colored cyan) staining on the cerebrum directly exposed to the BTIM and the cerebrum sham. (orange inset: sham group; blue inset: BTIM group). **Bioresorbable optical filters. g,** Cross-sectional illustration of a bioresorbable optical filter secured on an exposed region of the brain by the BTIM. **h,** Images to illustrate stable positioning of the filter by use of the BTIM with the encapsulation strategy. **i,** Transmission spectrum of a BTIM-encapsulated, bioresorbable optical filter. **Adhesive conduits for interconnects/cables. j,** Schematic illustrations of an adhesive 'tunnel', or conduit, that anchors the interconnects/cables onto tissues but allows their free motion within. **k, l,** Images that illustrate stable positioning of an interconnect/cable by an adhesive conduit. The adhesive conduit allows for the interconnect/cable to be bent (inset in **k**) and stretched during normal use (**k**). $n = 3$ biologically independent animals in **a**-**f**.

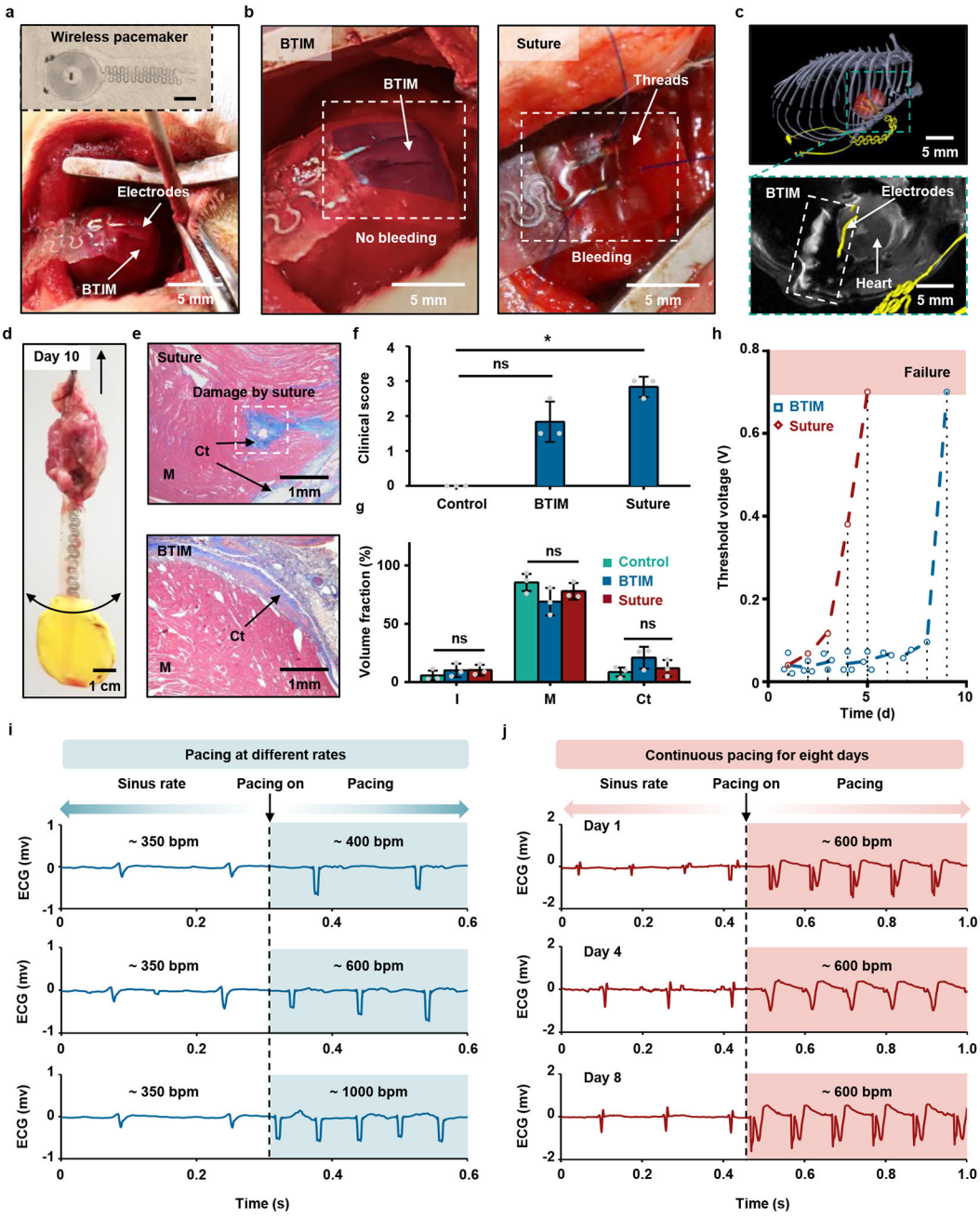

Fig. 5 |. Soft adhesive interfaces between wireless cardiac pacemakers and the myocardium for cardiac pacing.

a, Image of the pacemaker and the process of adhering the electrodes to the myocardium in a rat model using the encapsulation strategy. Inset: thin, flexible wireless cardiac pacemaker that includes a radio frequency power harvester positioned in the lateral dorsal subcutaneous pocket, with a pair of pacing electrodes that attaches onto the anterior epicardial surface of the ventricles. **b,** Gentle, conductive, stable interface formed by BTIM (first panel; colored in blue) avoids tissue damage and bleeding that typically occurs with suturing (second panel). **c,** Positions of the electrodes and the BTIM illustrated with an

overlay of MRI with MicroCT images one week post-surgery. **d,** Manual mechanical tests demonstrate the strength of adhesion day 10 post-surgery. **e,** Representative images of Masson's trichrome stained cross-sections compare implants secured with sutures (first panel) and the BTIM (second panel). **f,** Significantly more disorganized connective tissue appears on top of the myocardium for pacemakers secured with sutures. Kruskal-Wallis test, $H(2) = 7.245$, $P = 0.0071$; Post-hoc Dunn's multiple comparison test, $P_{(\text{control vs BTIM})} = 0.4334$, $P_{(\text{control vs suture})} = 0.0215$. **g,** Masson's trichrome staining of the epicardium near the site of pacemaker attachment four weeks post-surgery for suture and BTIM methods quantifies insignificant changes in the volume fractions of interstitial space, myocardium, and fibrosis in cardiac cross-sections. Kruskal-Wallis test, $H(2) = 0.6222$, $P = 0.8286$. Post-hoc Dunn's multiple comparison test, $P > 0.9999$. **h,** Threshold voltages for pacing to compare pacemakers secured with sutures (red) and the BTIM (blue). (One of the two suture pacemakers failed to pace on day 1 post-surgery; dash lines indicate the average values on each day; dot lines indicate the operating day) **i,** Representative ECG recordings show conversion from normal sinus rhythm to pacing rates of ~ 400, 600, and 1000 bpm, respectively. **j,** Representative ECG recording at day 1, 4, and 8 after implantation. $n = 3$ biologically independent animals in **a-g**. Values in **f** and **g** represent the mean ± standard deviation. Statistical significance and P values are determined by Kruskal-Wallis test and Post-hoc Dunn's multiple comparison test at a significance level of 0.05. ns indicates no statistically significant differences; $*P < 0.05$.

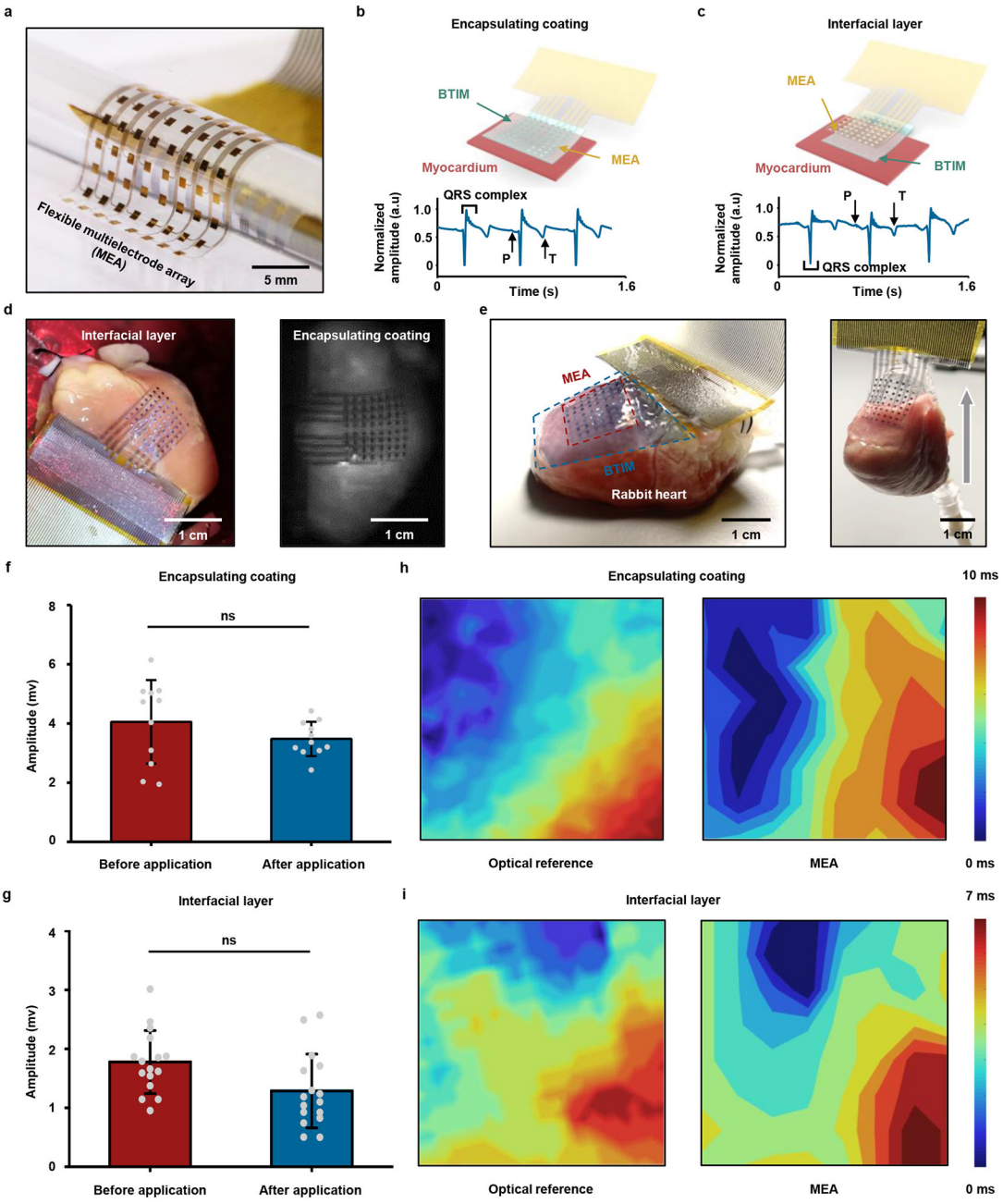

Fig. 6 |. Ultra-thin, flexible MEAs adhered to the epicardium.

a, Image of a MEA device designed for spatiotemporal mapping with 64 electrodes (8 columns, 8 rows). **b, c,** First panels: schematic illustrations of integration strategies based on the encapsulation (**b**) and the interface (**c**) schemes. Second panels: high quality normalized electrograms of sinus rhythms from a representative electrode in devices adhered using both of these methods. **d,** MEA configuration on the epicardial surface for both methods (first panel, encapsulating coating; second panel, interfacial layer). **e,** First panel: information on the positioning of the heart, electrode array, and the BTIM. Second panel: stable adhesion after 8 h of testing in the Langendorff perfusion system. **f, g,** Amplitudes of electrograms

recorded with devices after integration with the encapsulation (**f**) and interface (**g**) methods. The results are similar to those collected with devices held by capillary interaction ($P = 0.5195$ for encapsulating coatings and $P = 0.0507$ for interface layers). **h, i,** Strong spatial correlations of time coincident optical (first panel) and electrical activation maps (second panel) recorded with MEAs attached by the encapsulation (**h**) and interface (**i**) methods. $n = 11$ independent electrodes in **f** and $n = 16$ independent electrodes in **g**. Values in **f** and **g** represent the mean ± standard deviation. Statistical significance and P values are determined by Wilcoxon matched pairs signed-rank test at a significance level of 0.05. ns indicates no statistically significant differences.